Cu-doping of calcium phosphate bioceramics: From mechanism to the control of cytotoxicity

Sandrine Gomes, C. Vichery, Stéphane Descamps, Hervé Martinez, Amandeep Kaur, Aurélie Jacobs, Jean-Marie Nedelec, Guillaume Renaudin

Cu-doping of calcium phosphate bioceramics: from mechanism to the control of cytotoxicity

Sandrine Gomes[1], Charlotte Vichery[1], Stéphane Descamps[1], Hervé Martinez[2], Amandeep Kaur[1#], Aurélie Jacobs[1], Jean-Marie Nedelec[1], Guillaume Renaudin[1*]

[1] Université Clermont Auvergne, CNRS, SIGMA Clermont, ICCF, F-63000 Clermont-Ferrand, France.

[2] Université de Pau et des Pays de l'Adour, IPREM CNRS UMR 5254, Helioparc Pau Pyrénées, 2 Avenue de Président Angot, F-64053 Pau Cedex 9, France.

[*] corresponding author: guillaume.renaudin@sigma-clermont.fr

Tel.: 00 33 4 73 40 73 36, Fax.: 00 33 4 73 40 70 95

[#] Present address: VIT University, Vellore, Tamil Nadu 632014, India.

Abstract:

In this study, the Cu-doping mechanism of Biphasic Calcium Phosphate (BCP) was thoroughly investigated, as was its ionic release behavior, in order to elucidate cytotoxicity features of these bioceramics. BCP are composed of hydroxyapatite ($Ca_{10}(PO_4)_6(OH)_2$) and β-TCP ($Ca_3(PO_4)_2$). The two phases present two different doping mechanisms. Incorporation into the β-TCP structure is achieved at around 700°C thanks to a substitution mechanism leading to the Cu-doped $Ca_{3-x}Cu_x(PO_4)_2$ compound. Incorporation into the HAp structure is achieved thanks to an interstitial mechanism that is limited to a Cu-poor HAp phase for temperatures below 1100°C ($Ca_{10}Cu_x(PO_4)_6(OH)_{2-2x}O_{2x}$ with $x < 0.1$). Above 1100°C, the same interstitial mechanism leads to the formation of a Cu-rich HAp mixed-valence phase ($Ca_{10}Cu^{2+}_xCu^{+}_y(PO_4)_6(OH)_{2-2x-y}O_{2x+y}$ with $x+y \sim 0.5$). The formation of both high-temperature Cu-doped α-TCP and $Cu_3(PO_4)_2$ phases above 1100°C induces a transformation into the Cu-rich HAp phase on cooling. The linear O-Cu-O oxocuprate entity was confirmed by EXAFS spectroscopy, and the mixed Cu^+/Cu^{2+} valence was evidenced by XPS analyses. Ionic releases (Cu^+/Cu^{2+}, Ca^{2+}, PO_4^{2-} and OH^-) in water and in simulated body media were investigated on as-synthesized ceramics to establish a pretreatment before biological applications. Finally the cytotoxicity of pretreated disks was evaluated, and results confirm that Cu-doped BCP samples are promising bioceramics for bone substitutes and/or prosthesis coatings.

Keywords: Copper-doping, Hydroxyapatite, X-ray Diffraction, X-ray Absorption Spectroscopy, X-ray Photoelectron Spectroscopy, Cytotoxicity.

1- Introduction

The utilization of synthetic materials for bone reconstructive surgery is generally necessary, because autograft and allograft practice is limited by the quantity of available material and entails a second surgical procedure in the first case [1]. Among the numerous synthetic materials investigated for bone replacement and/or prosthesis coating, hydroxyapatite (HAp, $Ca_{10}(PO_4)_6(OH)_2$) is the most often-used material due to its chemical and structural similarities with the bone mineral constituent [2-5]. Biological apatite refers to the main constituent of bone and hard tissue in mammals: a poorly crystallized non-stoichiometric carbonate-containing HAp that composes about 65 weight percent (wt %) of bone and about 90 wt % of dental enamel [6]. Apatite is a complex and diverse class of materials, with a flexible structure that accepts many substitutions; either cationic or anionic [7]. Because biological apatites are formed in biological conditions, they usually contain a large variety of trace elements (F, Si, Sr, Mg, etc.) that can have specific biological properties. The incorporation of selected doping elements can be used advantageously to tune the bioactivity of the implant: antibacterial, anti-inflammatory, anti-osteoporotic or angiogenic properties, for instance. Biphasic calcium phosphates (BCP) are composed of a mixture of HAp with tricalcium phosphate (β-TCP, $Ca_3(PO_4)_2$). BCP are interesting bioceramics because of the difference in the solubility of the two compounds, which allows the kinetic release of the doping elements to be regulated. A fast release occurs with β-TCP immediately after a surgical operation, whereas a continuous effect is then ensured with HAp. Our previous studies have described in detail the temperature-dependent mechanism of Zn^{2+} insertion in BCP bioceramics [8-10]. Contrary to previous reports in the literature, Zn^{2+} incorporates the HAp structure into an interstitial crystallographic site (Wyckoff site 2*b*) leading to an insertion solid solution of general composition $Ca_{10}Zn_x(PO_4)_6(OH)_{2-2x}O_{2x}$ with a constant Ca/P ratio of 1.67. The insertion of Zn^{2+} is performed for temperatures above 900°C. For lower temperatures, Zn-doping is mainly efficient for the β-TCP phase, evincing a calcium substitution mechanism $Ca_{3-x}Zn_x(PO_4)_2$. Recent works on Fe-doping have confirmed this

temperature-dependent process leading to a HAp interstitial mechanism for temperatures above 900°C [11]. A complete study of 3d-metal cation (from Mn to Zn) incorporation in BCP has confirmed a global equivalent doping mechanism with interesting characteristics [12]. In order to perfectly interpret the biological behavior of doped bioceramics, it is of great importance to correctly characterize the structural location of the doping elements. Metal ions such as Zn^{2+}, Cu^{2+} and Ag^{+} are known not to be cytotoxic at low concentrations, and to exhibit antimicrobial/bactericidal activity at the site of the implantation materials [13-19]. However, the biological responses of the dopant strongly depend on its release amount and kinetic [20]. Jin et al. published last year a review of the development of bio-functional Cu containing biomaterials (including copper-doped HAp), illustrating the renewed interest in copper bioactivity [21].

The present study aims to fully investigate the Cu-doped BCP system. Besides its antimicrobial activity, copper is an essential trace element, necessary for mammalian life [22] and it plays a role in the cross-linking of collagen and bone elastin [23-25]. Cu^{2+} ions have been reported to enhance angiogenesis potential, osteostimulation and antibacterial properties [26-28], to stimulate the proliferation of endothelial cells [29], to promote wound healing in rats [30,31], and to enhance cell activity and the proliferation of osteoblastic cells [32]. A recent study on copper containing glass-ceramic has shown the interesting potential of Cu^{2+} doping for bioactivity and biocompatibility, with the necessity to control the CuO content, i.e. to manage Cu^{2+} release, in order to tune activity and viability [20,33]. Several hydroxyapatite copper doping mechanisms have so far been described in the literature. Whereas some authors have presented a substitution mechanism [34-36], others have described an insertion mechanism with the formation of linear O-Cu-O entities [12,37-39] and the possible presence of mixed Cu^{+}/Cu^{2+} valence. It is necessary to investigate in detail and correctly describe the mechanism of incorporating copper into BCP in order to 1/ adequately prepared the doped ceramic, and 2/ understand and tune the biological behavior of Cu-doped BCP bioceramics. Our prepared Cu-

doped disks were evaluated with respect to ionic release in simulated biological media (DMEM), and in terms of cytotoxicity using human mesenchymal cells in order to be close to clinical conditions.

2- Materials and methods

2.1 Sol-gel elaboration of Cu-doped BCP samples

The sol-gel route previously proposed by the authors was used to synthesize both undoped and Cu-doped series of BCP samples [8]. Briefly, to produce 2 g of undoped BCP powder, 4.7 g of $Ca(NO_3)_2.4H_2O$ (Aldrich) and 0.84 g of P_2O_5 (Avocado Research chemicals) were dissolved in ethanol under stirring and refluxed at 85°C for 24 hours. The solution was then maintained at 55°C for 24 hours to obtain a white consistent gel, and further heated at 80°C for 10 hours to obtain a white powder. Finally, the powder was heat-treated for 15 hours. This heat treatment was performed at 500°C, 600°C, 700°C, 800°C, 900°C, 1000°C, 1100°C, 1150°C and 1200°C. Required amounts of $Cu(NO_3)_2.3H_2O$ (Sigma-Aldrich) were added to the solution simultaneously with $Ca(NO_3)_2.4H_2O$ (Sigma-Aldrich) in order to synthesize the Cu-doped series. To obtain a series of nine samples with the same copper-containing amount, a single batch was prepared for each series and used for all the subsequent heat treatments. Nominal compositions were calculated, assuming the insertion of Cu^{2+} cations in the interstitial crystallographic site (i.e. Ca/P = 1.67), similarly to previous results for the Zn^{2+} insertion mechanism [8-10]. In the following, the samples are labelled '*x*Cu-*T*' with *x* = 00, 10, 15, 25, 50 and 75 for samples with respectively the targeted nominal $Ca_{10}(PO_4)_6(OH)_2$ (i.e. undoped), $Ca_{10}Cu_{0.10}(PO_4)_6(OH)_{1.80}O_{0.20}$, $Ca_{10}Cu_{0.15}(PO_4)_6(OH)_{1.70}O_{0.30}$, $Ca_{10}Cu_{0.25}(PO_4)_6(OH)_{1.50}O_{0.50}$, $Ca_{10}Cu_{0.50}(PO_4)_6(OH)_{1.00}O_{1.00}$ and $Ca_{10}Cu_{0.75}(PO_4)_6(OH)_{0.50}O_{1.50}$ compositions. In this label, *T* indicates the sintering temperature. More than 50 samples were prepared and characterized. A low-doped 10Cu-*T* series was used for dopant release and cell viability studies. Elemental analyses of the samples by ICP-AES confirmed the targeted nominal compositions. Sample

color is sintering-temperature dependent. As-prepared powders obtained after the sol-gel process were blue. Heat treatments at 500°C produced grey samples: from light grey to dark grey as the amount of copper increased. Samples still had a grey color up to 1000°C, and became purple from 1100°C. Finally, heat treatments at 1200°C resulted in dark purple powders.

2.2 X-Ray Powder diffraction (XRPD) and Rietveld analyses

XRPD patterns were recorded on a Philips X'Pert Pro PANalytical diffractometer (Almelo, Netherlands), with θ-θ geometry, reflection mode, equipped with a solid detector X-Celerator and using Cu Kα radiation (λ = 1.54184 Å). XRPD patterns were recorded at room temperature in the interval $3° < 2\theta < 120°$, with a step size of $\Delta 2\theta = 0.0167°$ and a counting time of 200s for each data value. The 45 synthesized samples from series 00Cu-*T*, 15Cu-*T*, 25Cu-*T* and 75Cu-*T* series were systematically analyzed by XRPD in reflection mode.

Two supplementary measurements were collected for samples 75Cu-1100 and 75Cu-1200 using Debye-Scherrer geometry (transmission mode) to improve diffraction peak resolution (2 theta resolution). Transmission measurements were recorded using a Philips X'Pert Pro diffractometer equipped with a Ge hybrid monochromator (Cu $K\alpha_1$ = 1.54056 Å). A total counting time of 40 hours was used in the range $3° < 2\theta < 120°$, with a step size of $\Delta 2\theta = 0.0167°$, using a 0.3 mm diameter filled glass capillary.

In-situ temperature-dependent XRPD patterns were recorded for the 75Cu-*T* series. XRPD patterns were collected on a Philips X'Pert Pro diffractometer equipped with a high-temperature HTK chamber (Anton Paar, Graz, Austria) with the following measurement conditions: two theta range $8° < 2\theta < 100°$, step size $\Delta 2\theta = 0.0167°$, time per step = 165 s. A series of diffraction patterns was recorded, from 500°C up to 1200°C (using the starting 75Cu-500 sample). Data were collected at 500°C, 600°C, 700°C, 800°C, 900°C, 1000°C, 1100°C, 1150°C and 1200°C. Then data measurements were performed during the cooling from 1200°C to room temperature: 1150°C, 1100°C, steps of 100°C down to 100°C and finally 25°C.

Rietveld refinements were systematically performed for each measurement using the program FullProf.2k [40]. The Rietveld strategy was detailed in a previous related work [8].

2.3 X-ray Absorption Spectroscopy (XAS)

Cu K-edge Extended X-ray Absorption Fine Structure (EXAFS) spectra, simultaneously with the X-ray Absorption Near Edge Structure (XANES) part of the spectra, were collected on the Cu-doped samples from the 15Cu-*T* series and one reference compound (CuO) at the SuperXAS beam line at the SLS synchrotron (Villigen, Switzerland) in order to determine the electronic state, as well as to describe accurately the coordination spheres of the Cu atoms. Samples from the 15Cu-*T* series were chosen because other series present higher amounts of CuO impurities. The SLS synchrotron was running at 4.5 – 35 keV with an average current of 400 mA. The X-ray beam was obtained with a two-crystal Si(111) monochromator, which features an energy resolution of $\Delta E/E = 2.0 \times 10^{-4}$, necessary to resolve the XANES structure. The experiments were calibrated using a Cu metallic reference foil (K-edge 8981 eV). Experiments were performed at room temperature and atmospheric pressure. Spectra were collected in an energy range of between 8500 and 9500 eV, with energy steps varying from 0.5 eV (XANES part) to 2.0 eV (end of the EXAFS part) and a 1s dwell time per point. XAS spectra were obtained in fluorescence mode using Ge-solid-state detectors (13-element detector). The size of the beam was determined by a set of slits (200 μm x 500 μm). Data was processed using the Athena and Artemis programs from the IFFEFIT software package [41] by merging 4 successively-recorded absorption spectra. Single scattering theory was used here. Following Lengeler-Eisenberg normalization, EXAFS oscillations were Fourier Transformed (FT) using a Hanning window between 3.0 and 9.0 $Å^{-1}$. The $\chi(k)$ function was Fourier transformed using k^3 weighting, and all shell-by-shell fitting was done in *R*-space. Theoretical backscattering paths were calculated using successively ATOMS [42] and FEFF6 [43].

2.4 X-ray Photoelectron Spectroscopy (XPS)

XPS measurements were carried out to determine the mean oxidation state of Cu with a Thermo Scientific K-Alpha X-ray photoelectron spectrometer using focused monochromatized Al Kα radiation (hν = 1486.6 eV). The XPS spectrometer was directly connected through a glove box under argon atmosphere in order to avoid exposing the samples to moisture or air. For the Ag 3d5/2 line the full width at half-maximum (FWHM) was 0.50 eV under the recording conditions. The X-ray spot size was 400 μm. Peaks were recorded with a constant pass energy of 20 eV. The pressure in the analysis chamber was less than 1×10^{-8} Pa. Short acquisition time spectra were recorded at the beginning and at the end of each experiment to check that the samples did not suffer from degradation during the measurements. Peak assignments were made with respect to reference compounds analyzed in the same conditions. The binding energy scale was calibrated from the hydrocarbon contamination using the C 1s peak at 285.0 eV. Core peaks were analyzed using a nonlinear Shirley-type background [44]. The peak positions and areas were optimized by a weighted least-square fitting method using 70% Gaussian and 30% Lorentzian line shapes. Quantification was performed on the basis of Scofield's relative sensitivity factors [45]. For each sample, several XPS analyses were performed at different positions to ensure that the results were statistically reliable.

2.5 MP-AES measurements

Ionic releases in both water and a culture medium used to simulate body fluid (DMEM; Dulbecco Modified Eagle Medium) were measured by Microwave Plasma - Atomic Emission Spectroscopy (4200 MP-AES from Agilent) in order to evaluate the behavior of the Cu-doped bioceramic in solution, and to determine the pretreatment of Cu-doped BCP disks intended for biological applications. A series of calibration samples was prepared using a 1000 μg/mL Cu ion normadose (diluted in 5% HNO_3 solutions, distributed by Agilent Technologies), diluted in

a solvent similar to those of the solutions measured, which is to say 1/1 ratio for DMEM/HNO_3 2% and ultra-pure water/HNO_3 2% solutions.

2.6 Cytotoxicity evaluation

Following the BCP structural characterization, the 10Cu-*T* (*T* = 600, 900 and 1200°C) samples were prepared for cytotoxicity assessment and undoped copper-free samples were used as reference. The 10Cu-*T* series was chosen because of the absence of copper oxide impurities (see Table 1). Cell viability was assessed through a cell count after a period of cell culture on the studied material (using flat pressed disks). All conditions were tested in triplicate.

2.6.1 Bone Marrow Cell (BMC) preparation: human normal bone marrow cell source, isolation and in-vitro expansion of BM mesenchymal cells before use.

Human BMC were obtained from metaphysal cancellous bone collected during hip arthroplasty. Pieces of femoral metaphysis cancellous bone were gathered during surgical procedures in patients who had signed an authorization for the use of their bone for research purposes. All donors had normal hematopoietic function. The samples were collected in a sterile culture medium (αMEM) and transported immediately to the culture lab. After washing once in phosphate-buffered saline (PBS) 4% fetal calf serum (FCS), the BMC were re-suspended in a standard marrow cell culture medium consisting of αMEM 10% FCS, 100 U penicillin, 100 µg/mL streptomycin, 2 mM L-Glutamin and plated at 1.5 x 10^5 cells/cm^2 in 25 cm^2 tissue culture flasks at 37°C with 5% of humidified CO_2 for two days. The non-adherent BMC were harvested in two gentle rinses and removed. Adherent cells were fed by a weekly change of medium. Mesenchymal cells were expanded through one of three passages (re-plated between 5 x 10^2 and 1 x 10^3 cells/cm^2) before being collected by trypsinization.

2.6.2 Assessment of mesenchymal cell proliferation on samples disks.

Sterilization of each disk was completed with a sequence of ethanol (95%) for 30 minutes followed by PBS for 30 mins; this was performed twice. The disks were placed in 24-well cell culture trays, with 8 x 10^3 cells/well seeded in each well. One disk per well was plated in triplicate in 24-well plates to produce a representative series. Each disk was sowed with the same number of expanded mesenchymal cells (8 x 10^4 cells) in a standard medium with 700 µL of medium in each, which was changed twice weekly. All disks were colonized by cells coming from the same patient during the same expansion process.

To evaluate cell viability, the wells were sacrificed to collect cells after one week of culture. Cells were harvested after detachment by trypsin/EDTA 0.25% and counted in Malassez. For each arm, we evaluated in parallel the viability of cell proliferation on equivalent uncoated plastic wells in the absence of a disk as a control, in order to estimate the effect of ceramic disks only. One extra disk was seeded in the same way and sacrificed at day 6 to study cell morphology using SEM.

2.6.3 Statistical analysis.

Results were expressed as means ± standard error of mean, considering triplicate samples. Limiting Dilution Analysis (LDA) was performed according to the Poisson statistical model using L-Calc™ software (StemCell Technologies, Vancouver, Canada). Statistical analysis used the bilateral paired Student's test with a significant p value < 0.05.

3- Results: Materials characterization

3.1 Temperature-dependent phase composition of the samples

To correctly interpret the behavior of our samples, their mineral compositions were extracted from Rietveld analyses (selected XRPD patterns are shown in Figure SEI1). Mineral compositions of the undoped BCP series and of the four Cu-doped BCP series (x = 15, 25, 50 and 75) of samples are indicated in Table 1. Results are extracted from XRPD measurements performed with the θ-θ geometry except when indicated by an asterisk (transmission mode on

capillary) in Table 1 and Table SEI1. Figure 1 represents the thermal composition variation for the two main phases: HAp and β-TCP. Other minor phases were observed. α-CDP (diCalcium DiPhosphate with composition $Ca_2P_2O_7$) was observed up to 700°C, with a maximum amount – around 6-9 wt % – at 600°C. Calcite $CaCO_3$ was present in samples which were heat treated at 500°C, and decarbonation mainly occurred at 600°C. CuO was generally observed in samples from the Cu-doped series – except for 15Cu-1150 and 15Cu-1200 (which are composed of HAp and β-TCP only) – indicating that part of the incorporated copper amount is not inserted in the two main phases. β-TCP was stabilized for intermediate temperatures and the presence of copper increased the β-TCP amount at 700°C. Samples became almost exclusively composed of HAp phases for the higher temperatures, except for the 15Cu-*T* series with about 10 wt % of β-TCP remaining above 1000°C.

Thermal variations in the HAp lattice parameters (Figure 2 and Table SEI1) showed only minor variations between undoped and Cu-doped series from 500°C up to 1100°C (the maximum heat treatment usually used in our previous studies on BCP doping [8-12, 46-48]). Weak copper insertion into the interstitial 2*b* Wyckoff site was observed up to 1100°C from Rietveld refinements on samples belonging to the four Cu-doped series: between 1 and 5 % occupancies leading to a maximum inserted copper composition $Ca_{10}Cu_{0.1}(PO_4)_6(OH)_{1.8}O_{0.2}$ for the 50Cu-1100 sample (Table SEI1). The *a* lattice parameter of Cu-doped samples heat treated at temperatures between 500°C and 700°C shows a decrease compared to the undoped series (Figure 2). Attempts to substitute calcium atoms during the Rietveld procedure (considering both the Ca1 and Ca2 crystallographic sites in the HAp structure [49]) failed, whatever the amount of copper and the sintering temperature. Higher-temperature treatments were performed (1150°C and 1200°C) in order to pursue the temperature-dependent study on copper insertion. For temperatures above 1100°C, lattice parameters sharply increased. These variations in the HAp unit cell were accompanied by a large increase in copper occupancy at the interstitial 2*b* Wyckoff site (Figure 2 and Table SEI1). More surprisingly, samples heat treated at 1150°C and

1200°C from the 50Cu-*T* and 75Cu-*T* series showed systematic shoulders for almost all diffraction peaks related to the HAp structure. Such behavior can be explained by the presence of two HAp phases with slightly different lattice parameters. Rietveld refinements were then performed on XRPD patterns recorded in transmission mode on capillaries filled with the two 75Cu-1100 and 75Cu-1200 samples in order to improve the diffraction peak resolution (Figure 3). The presence of two HAp phases was clearly evidenced. Results indicated that one phase (HAp1 in Figure 3) corresponding to the HAp phase observed in samples heat treated below 1100°C relates to the previously indicated composition $Ca_{10}Cu_{0.1}(PO_4)_6(OH)_{1.8}O_{0.2}$; called Cu-poor HAp phase hereafter. The second, and new, HAp phase (HAp2 in Figure 3) presents larger lattice parameters and a larger quantity of copper cations at the interstitial site, leading to the refined $Ca_{10}Cu_{0.6}(PO_4)_6(OH)_{0.8}O_{1.2}$ composition, called Cu-rich HAp phase hereafter. Figure 2 and Table SEI1 take into consideration the characteristics of these two HAp phases for the 50Cu-*T* and 75Cu-*T* series. Structural parameters of both Cu-poor and Cu-rich HAp phases from sample 75Cu-1200 are gathered in Table 2.

The main structural parameters of the β-TCP phase in samples from each series – containing the largest amount of β-TCP phase (800°C for the undoped series and 700°C for the Cu-doped series; see Table 1) – can be seen in Table SEI2. The substitution mechanism was evidenced by the decrease in the lattice parameters of its rhombohedral structure [51]. Refinement of the atomic occupancy factors showed that the substitution mechanism occurs in the low-density column [48] at both the Ca4 and Ca5 crystallographic sites – in agreement with previous observations on the transition metal insertion mechanism [8-12]. Maximum refined substitution led to the $Ca_{2.72(3)}Cu_{0.28(3)}(PO_4)_2$ composition for 75Cu-700 (Table SEI2). The literature already indicates the existence of $Ca_{19}Cu_2(PO_4)_{14}$ – polymorphic to β-TCP with the same rhombohedral *R*3*c* structure – very close to our refined composition [51]. Higher amounts of copper substitution lead to structure modifications: monoclinic $P2_1/c$ $Ca_{1.5}Cu_{1.5}(PO_4)_2$ [52] and triclinic $P\bar{1}$ calcium-free $Cu_3(PO_4)_2$ [53].

3.2 Formation of the second, copper-rich, HAp phase

In order to understand the formation mechanism of the two HAp phases for high sintering temperatures – the Cu-poor and the Cu-rich HAp phases – in-situ high-temperature XRPD measurements were performed on the 75Cu-*T* series. Rietveld refinements enabled the temperature-dependent quantitative phase analysis and the corresponding assemblage variation to be identified (Figure 4). The 75Cu-500 sample was introduced into the high-temperature HTK chamber, and XRPD patterns were recorded during heating from 500°C up to 1200°C and then during cooling down to room temperature. From 500°C to 1000°C, phase mixtures were coherent with those previously observed from measurements performed at room temperature on cooled samples: namely the stabilization of β-TCP observed around 700°C. Nevertheless, above 700°C the amount of β-TCP remained almost unchanged, and the amount of HAp increased, together with the consumption of copper oxide CuO. This last point was not evidenced from measurements carried out at room temperature on cooled samples, where the CuO amount remained constant at around 5 wt % (Table SEI1). Between 1000°C and 1100°C the β-TCP transformed into the α-TCP polymorph and the tri-copper phosphate, triclinic $Cu_3(PO_4)_2$, appeared [53]. Between 1100°C and 1200°C the β-TCP phase completely disappeared and the HAp phase was considerably destabilized (about 20 wt % only at 1200°C) to the benefit of α-TCP and $Cu_3(PO_4)_2$. Minor changes were observed during cooling from 1200°C and 1100°C. At 1000°C, both α-TCP and $Cu_3(PO_4)_2$ phases disappeared, concomitantly with a large increase in the HAp phase and the formation of about 10 wt % of the β-TCP polymorph. Because of the relatively low 2-theta resolution of the XRPD patterns recorded using the HTK chamber, Rietveld refinements did not enable us to discriminate clearly the presence of two HAp phases. Cooling from 1000°C to room temperature did not show a significant evolution. Nevertheless, information provided by these HTK measurements indicated that the Cu-rich HAp phase came from the transformation of both α-TCP (certainly

copper substituted) and $Cu_3(PO_4)_2$ phases between 1200°C and 1100°C. This transformation, performed above 1100°C, explained the absence of the Cu-rich HAp phase for heat treatments up to 1100°C (Figure 2). The presence of both HAp1 and HAp2 phases in Figure 4 during cooling was extrapolated from previous transmission results.

3.3 Copper location in the HAp structure

During Rietveld refinements the occupancy factors of all calcium and phosphorus crystallographic sites were systematically tested, as well as the eventual copper substitutions at calcium sites (two crystallographic sites for HAp and five crystallographic sites for β-TCP) and copper insertion at the interstitial 2*b* Wyckoff site. Results indicated, as already thoroughly described for Zn^{2+} doping, that the mechanism is temperature-dependent with a first step around 700°C corresponding to a substitution mechanism in the *β*-TCP phase, followed by an insertion mechanism in the HAp phase. The latter is fully accomplished for sintering temperatures higher than 1100°C to obtain the Cu-rich HAp phase with the $Ca_{10}Cu_{0.6}(PO_4)_6(OH)_{0.8}O_{1.2}$ composition. In order to confirm this insertion mechanism, XAS analyses were performed on five samples from the 15Cu-*T* series (15Cu-500, 15Cu600, 15Cu-800, 15Cu-1100, 15Cu-1200 samples: Figure SEI2) at the SuperXAS beam line at the SLS synchrotron (Villigen, Switzerland). Samples from the 15Cu-*T* series were chosen because of the lower amounts of CuO impurity for all samples of the series (less than 1 wt % and total absence for 15Cu-1200; see Table1). EXAFS spectra were expected to enable us to evidence the formation of linear O-Cu-O entities with short Cu-O interatomic distances. Previous Rietveld refinements did not allow this short Cu-O interatomic distance to be determined because of statistical disorder around the oxygen atoms in the HAp hexagonal channel: the O4 crystallographic site corresponds either to oxygen from isolated hydroxyl groups or to oxygen from linear O-Cu-O entities. Rietveld analyses indicated only the wide 1.40-2.05 Å range for the Cu-O interatomic distance. Fourier-transformed amplitudes (not corrected for phase shift) are shown in Figure 5b in *R*-space. Radial

distributions for the different samples did not show great variations, and were relatively similar to that of the CuO reference compound in the 1 Å – 3 Å *R* range. It should be remembered that samples were not single-phase, and several phases contribute to the spectra: copper from CuO impurity, substituted copper in *β*-TCP and inserted copper in HAp. Nevertheless, careful analysis of the radial distribution showed that the first peak is slightly displaced toward the small *R* values for the 15Cu-1200 sample: 1.48 Å against 1.51 Å for other 15Cu-*T* samples and for the CuO reference compound. 15Cu-1200 is the only sample without any CuO impurity. Fitting the k^3-weighted EXAFS raw data of 15Cu-1200 (Figure SEI3) confirmed the two oxygen neighbors and indicated a refined Cu-O interatomic distance of 1.91 (1) Å. This relatively short interatomic distance (compared to d_{Cu-O} = 1.96 Å in CuO) agrees with the insertion mechanism of copper cations at the 2*b* interstitial Wyckoff site, leading to linear O-Cu-O oxocuprate. The XANES part of the spectra (Figure 5a) showed the appearance of a pre-edge peak at 8983 eV from a sintering temperature of 1100°C: a shoulder for the 15Cu-1100 sample and a sharp pre-edge signal for the 15Cu-1200 sample. Analysis of the EXAFS data is a direct method that probes the electronic and structural nature of the metal site [54-56]. Empirical correlations of the energies of copper X-ray absorption edge features were used to detect the presence of Cu^+. It was recognized that the pre-edge feature at 8983 eV is present in the absorption edge spectra of Cu^+ complexes but not in those of Cu^{2+}. Kau and al. have shown that samples containing Cu^+ exhibit a near-edge absorption feature at 8983.5(3) eV, consistent with the 1s–4p transition of a Cu^+ center, whereas Cu^{2+} entities do not exhibit a peak below 8985 eV [57]. Cu^{2+} cations are characterized by a broader signal [58]: the shoulder of the Cu Kα edge observed in Figure 5a for the CuO reference compound and for samples 15Cu-500, 15Cu-600 and 15Cu-800.

3.4 Cu⁺/Cu²⁺ mixed valence in HAp above 1100°C

Samples from the 75Cu-T series were analyzed by XPS spectroscopy in order to confirm the presence of Cu^{+} cations for heat treatments above 1100°C. XPS spectra ($2p_{3/2}$) from samples 75Cu-1000 to 75Cu-1200, presented in Figure 6, have been interpreted according to literature peak assignments described in Comment SEI1 from supplementary information section [59-62]. The Cu^{+}/Cu^{2+} ratio was estimated for the three samples considering the following conditions (based on the spectral analyses of the reference compounds): the binding energy for Cu^{+} is positioned at 932.7 eV and the associated component presents a constant full width at half maximum (FWHM) of 1.3 eV for the three samples. Furthermore, the relative proportion of Cu^{2+} for the 75Cu-1000, 75Cu-1100 and 75Cu-1200 samples could be also estimated by taking into account the ratio between the main Cu $2p_{3/2}$ peak and the corresponding satellite peaks located in the range 940-945 eV. The Cu^{+} amount is weak for 75Cu-1000 (Figure 6) with an experimental Cu^{+}/Cu^{2+} ratio of 0.03. This ratio increases to 0.10 for 75Cu-1100 and to 0.24 for 75Cu-1200. Note that for the last compound (75Cu-1200), the experimental envelope of the $2p_{3/2}$ component presents a shoulder at low binding energy. Furthermore, the ratio between the Cu^{2+} $2p_{3/2}$ contribution and the associated satellite peaks is lower than for 75Cu-1000 and 75Cu-1100, which is in agreement with a higher proportion of Cu^{+} in the 75Cu-1200 sample.

Thus XPS reveals the partial Cu^{2+} reduction for temperatures above 1100°C, and indicates that Cu^{+} is inserted in the Cu-rich HAp phase. Only about 16 atomic % of copper is in the Cu^{+} oxidation state in 75Cu-1200, indicating that the Cu-rich HAp phase did not contain exclusively Cu^{+}. The Cu-rich $Ca_{10}Cu_{0.6}(PO_4)_6(OH)_{0.8}O_{1.2}$ is a mixed-valence Cu^{+}/Cu^{2+}-doped HAp. It should be borne in mind that XPS is a surface analysis (depth analysis about 5 nm) and that results are not necessarily bulk representative. The main and significant XPS result here is the confirmation of the Cu^{+} electronic state, in agreement with XANES observation and the evidence of sintering temperature-dependence.

4- Results: Material behavior in a biological medium

4.1 Ionic release

The impact of the release of copper ions on cytotoxicity was studied for the 10Cu-*T* series, with *T* = 600, 900, and 1200°C. For comparison, measurements were also performed with the undoped series. Samples with a nominal composition of $Ca_{10}Cu_{0.10}(PO_4)_6(OH)_{1.80}O_{0.20}$ were selected because of the absence of copper oxide impurities previously observed in the 15Cu-*T* series, and because too high a quantity of copper ions released could indeed increase cytotoxicity. In addition, samples heat-treated at the three temperatures (600°C, 900°C and 1200°C) were chosen in order to vary the disk composition, the copper location and the degree of oxidation of the copper ions. As shown, a higher annealing temperature induces a higher HAp/β-TCP ratio, which could give rise to different copper ion release kinetics, the β-TCP phase being dissolved much faster than the HAp one.

To be close to cytotoxicity test experimental conditions, in a first experiment, each disk was immersed in 20 mL of a solution of simulated body fluid (DMEM – Dulbecco's Modified Eagle Medium, without D-Glucose and L-Glutamine). The closed bottles were maintained at 37°C in an oven, with 5% of humidified CO_2, for several days. As can be seen in Figure 7, after one day the concentration of copper ions in the solution was already high, and even reached 50 ppm after 21 days for the 900°C annealed sample. It is interesting to note that the Cu-doped BCP sample heat-treated at 1200°C shows a much lower copper ion release, which is directly correlated with its composition (no β-TCP phase and copper completely inserted in the weakly soluble HAp phase). The concentrations obtained, from 0.02 to 0.28 ppm for the undoped samples, confirm the non-contamination of these samples as well as the sensitivity of the measurements. During this experiment it was noticed that the pH of all the solutions significantly increased, probably due to the dissolution of the small amount of CaO in the samples. As such a pH increase could be harmful for the cell's viability in biological conditions, a post-synthesis treatment of the disks was performed in order to remove free CaO before

carrying out cytotoxicity measurements. In addition, it could be interesting to reduce the quantity of copper ions released, as a high concentration could also damage the cells.

In a second experiment, in order to dissolve CaO and prevent a rise in pH during the cytotoxicity tests, each disk was immersed in 20 mL of ultra-pure water, in a closed bottle placed in an oven at 37°C (5% of humidified CO_2). For the 6 samples (from both undoped and 10Cu-*T* series) the pH increased, reaching about 11.7 after 24 hours, proof of CaO dissolution. Surprisingly, almost no Cu ions were released, their concentration in water being less than the detection limit of the MP-AES (~0.01 ppm). The disks were then dried and immersed again for 24 hours at 37°C in ultra-pure water to ensure the complete dissolution of CaO. Then the disks were immersed in DMEM for 24 hours at 37°C, following the same protocol. The pH was measured and shown to be equal to that of pure DMEM after 24 hours at 37°C. Contrary to the treatment in water, copper ions were released in DMEM, their concentration reaching 16.7, 17.2 and 3.0 ppm respectively for 10Cu-600, 10Cu-900 and 10Cu-1200 samples. Copper ion concentration was finally measured after a second treatment of 24 hours in DMEM, and showed a release of 3.0, 6.6 and 0.4 ppm for 10Cu-600, 10Cu-900 and 10Cu1200 samples respectively, far less than the concentration obtained from the first experiment, with no post-treatment of the samples. Figure SEI4 illustrates these two experiments, and the corresponding disk preparations for the three cytotoxicity evaluation campaigns (0, A and B).

4.2 Cytotoxicity evaluation

Three cytotoxicity (i.e. cell viability) evaluation campaigns were conducted: first, experiments with disks from as-synthesized pressed powder (campaign 0; 13 mm diameter disks obtained with 0.25g of powder pressed under 1 ton using three *x*Cu-*T* series with x = 00, 10 and 25); and second, experiments with disks post-treated by two water immersions (campaign A) and with a third DMEM immersion (campaign B). Thus, for both campaigns, the pH should not rise during the cytotoxicity tests and different copper ion concentrations can be tested, campaign A

showing a higher Cu ion release compared to campaign B. In addition to the 10Cu-600, 10Cu-900 and 10Cu-1200 samples, post-synthesis treatments were performed on the 00Cu-600, 00Cu-900 and 00Cu-1200 samples, in order to have copper-free reference samples for the cytotoxicity interpretation. Results from the three evaluation sets (described in Figure SEI4) are shown in Figure 8. For each campaign, one 24-well plate was used with all the composition/sintering temperatures in triplicate, including controls corresponding to disk-free wells. We did not note any bacterial contamination during the culture period. Control measurements were 24-well plate-dependent with viable cell count values from 7.6 10^3 to 2.5 10^4 cells/well. In order to easily compare measurements from different campaigns, control results were normalized to 100 (then applying the same scale factor for all the measurements from the same 24-well plate; cytotoxicity values should be understood as a percentage of cell viability).

Campaign 0 with as-prepared disks evidences the dramatic impact of pH increase due to small amounts of free CaO in the sample (Figure 8a). In the presence of disks, undoped or Cu-doped, cell viability was continuously below the control with five samples around or (largely) below 20% cell viability. Nevertheless it is complicated to advance general observations from campaign 0. For a sintering temperature of 600°C, copper incorporation dramatically reduces cytotoxicity from about 50% (00Cu-600) to about 5% (25Cu-600). A similar trend was observed for a sintering temperature of 900°C, with slightly improved values (from about 65% for the 00Cu-900 sample to about 20% for the 25Cu-900 sample). For a sintering temperature of 1200°C, the case was completely different, with an improvement in cell viability in the presence of copper (from about 20% for undoped 00Cu-1200 sample to 50% for Cu-doped samples). This toxic behavior of the disks cannot be attributed solely to the presence of lime. The amount of CaO increases with copper insertion for heat treatment at 600°C (1.0 wt% of CaO for 00Cu-600 against 1.5 wt% for 25Cu-600; Table 1). Nevertheless, CaO was negligible with copper insertion at 900°C (0.2 wt% for 00Cu-900 and 0 wt% for (25Cu-900), and had

completely disappeared from the samples at 1200°C. Certainly the CaO and CuO combination should be considered to explain the toxicity of the disks prepared with as-synthesized powders. In fact, the first experiments on copper releases showed rapid and large copper concentrations in DMEM (more than 50 ppm, Figure 7).

Campaigns A and B still showed complex behaviors, although with better results in terms of cell viability (Figure 8b), indicating the beneficial effect of the disk post-treatments. In general, measurements from these two campaigns showed good cell viability at one week with respect to the control wells. For two samples only, the benefit of post-treatment was not observed: cell proliferation dropped for 00Cu-600 and there was no effect for 00Cu-900. Moreover, cell proliferation was clearly improved for the Cu-containing samples (10Cu-600, 10Cu-900 and 10Cu-1200). Again, the comparison between campaigns A and B does not enable obvious general guidelines to be drawn up. Campaign A seems favorable for samples 10Cu-600 and 10Cu-1200, whereas campaign B seems favorable for sample 10Cu-900. Figure 8b also highlights the favored proliferation for cells in contact with ceramics sintered at 1200°C. It is clear from these three cytotoxicity evaluation campaigns that controlling the preparation conditions (composition, temperature and post-treatment) makes it possible to increase cell viability in the vicinity of the ceramic. As an example, cell viability doubled with the 00Cu-1200 ceramic post-treated by water immersion.

5- Discussion

The copper incorporation mechanism in BCP samples presents similarities with the temperature-dependent mechanism previously described in the case of Zn-doping [8-10] and Fe-doping [11]. The main outlines of the temperature variations of the two HAp and β-TCP phases are extremely similar for the first row transition metal series from Mn to Zn [12]. Whatever the sintering temperature or the amount of incorporated copper, Rietveld refinement

did not show copper to calcium substitution in the HAp structure. Both Ca1 and Ca2 crystallographic sites of the HAp structure were tested: no copper substitution and no calcium deficiency were evidenced. This interstitial mechanism contradicts two earlier studies considering a substitution mechanism, carried out in 1989 on copper and zinc co-doped hydroxyapatite dried at 110°C only [35] and on copper-doped strontium substituted hydroxyapatite, heat-treated at 950°C [34]. The substitution mechanism was also mentioned in a recent study performed on copper-doped hydroxyapatite and fluorapatite, heat-treated at 700°C [36], although the indicated lattice parameters did not convincingly evince Vegard's law. On the other hand, the location of copper cations at the interstitial 2*b* Wyckoff site, along the HAp hexagonal channel, has already been reported. Crystallographic studies based on single crystal data indicated Cu atoms at the 2*b* site (0,0,0) with the formation of linear oxocuprate entities O-Cu-O in the belovite structure [63] and also in the hydroxyapatite structure [37]. EXAFS analysis of our samples confirmed the two-fold coordination for copper cations, with the d_{Cu-O} interatomic distance refined at 1.91 (1) Å. This value, greater than the previously determined d_{Zn-O} = 1.72 Å [10] and d_{Fe-O} = 1.84 Å [11], is certainly overestimated because of the presence of about 10 wt % of Cu-substituted β-TCP in the analyzed sample (15Cu-1200). For the lower sintering temperatures investigated in this study (below 1000°C), Cu-incorporation in the HAp phase is limited to the $Ca_{10}Cu_{0.05}(PO_4)_6(OH)_{1.90}O_{0.10}$ composition (Table SEI1). Heat treatment at 1100°C led to the refined $Ca_{10}Cu_{0.10(1)}(PO_4)_6(OH)_{1.80(2)}O_{0.20(2)}$ composition for the 50Cu-1100 sample (Table SEI1). The inserted metal cation amount at 1100°C is lower than that observed, in the same experimental conditions, for the Zn-doped series ($Ca_{10}Zn_{0.25}(PO_4)_6(OH)_{1.50}O_{0.50}$ [9]) or the Fe-doped series ($Ca_{9.75}Fe_{0.50}(PO_4)_6(OH)_1O_1$ [11]). An increase in sintering temperature, up to 1200°C, enables the $Ca_{10}Cu_{0.61(1)}(PO_4)_6(OH)_{0.78(2)}O_{1.22(2)}$ composition to be obtained (Table SEI1). Such a large amount of inserted copper is coherent with previous indications in the literature: $Ca_{10}Cu_{0.54}(PO_4)_6O_{1.72}H_y$ for a single crystal grown at 1300°C and slowly cooled to room

temperature [37], and $Ca_{10}Cu_{0.72}(PO_4)_6(OH)_{0.56}O_{1.44}$ for a powder sintered at 1100°C and air quenched [38]. To increase the copper occupancy factor from about 5% (corresponding to $Ca_{10}Cu_{0.10}(PO_4)_6(OH)_{1.80}O_{0.20}$: the Cu-poor HAp phase) to about 30% (corresponding to $Ca_{10}Cu_{0.60}(PO_4)_6(OH)_{0.80}O_{1.20}$: the Cu-rich HAp phase), it is necessary to apply temperatures greater than 1100°C. Above this temperature, the β-TCP phase and a large part of the hydroxyapatite are transformed into the α-TCP polymorph and tricopper phosphate $Cu_3(PO_4)_2$. We have shown that the copper-rich HAp phase, with composition $Ca_{10}Cu_{0.60}(PO_4)_6(OH)_{0.80}O_{1.20}$, is obtained during cooling by the transformation of both α-TCP polymorph and $Cu_3(PO_4)_2$ into a new copper-rich HAp phase (Figure 4). Contrary to the case of Zn^{2+}, oxocuprate insertion into the hexagonal channel led to an isotropic increase in the HAp unit cell volume (Figure 2). The insertion of linear O-Zn-O entities, at the same crystallographic site, induced an increase in the hexagonal *c* lattice parameter, concomitant with a decrease in the basal *a* lattice parameter [8-10], whereas we observe here a simultaneous increase in both the *a* and *c* lattice parameters of HAp. The comparison of Zn-doping and Cu-doping with equivalent doping levels shows relatively equivalent *c* values and very different *a* values: *a* = 9.4305 Å and *c* = 6.8959 Å (V = 531.12 $Å^3$) for $Ca_{10}Cu_{0.27(1)}(PO_4)_6(OH)_{1.46(2)}O_{0.54(2)}$ (Table SEI1) against *a* = 9.4077 Å and *c* = 6.9077 Å (V = 529.46 $Å^3$) for $Ca_{10}Zn_{0.26(1)}(PO_4)_6(OH)_{1.48(2)}O_{0.52(2)}$ [8]. The *a* lattice parameter of undoped HAp is intermediate, about 9.420 Å (Table SEI1). It indicates that O-Zn-O attracts adjacent phosphate groups, and this is not the case with the oxocuprate entity. Phosphate anions are localized at 2.96 Å from the inserted copper cations (through the O3 crystallographic site) while this distance is reduced to 2.92 Å in the case of zinc cations. In a manner similar to the Zn-doping case, β-TCP was stabilized for heat treatments at around 700°C. About 17 wt % of β-TCP is observed at 700°C (Table 1) with the formation of a Cu-substituted β-TCP phase with an average $Ca_{2.75}Cu_{0.25}(PO_4)_2$ composition (Table SEI2). The substitution occurs without structural modification, in agreement with literature. A change in symmetry is reported for

larger amounts of copper: a monoclinic $P2_1/c$ structure for the $Ca_{1.5}Cu_{1.5}(PO_4)_2$ compound [52]. The high-temperature tri-copper phosphate $Cu_3(PO_4)_2$ formed at 1100°C and above – which corresponds to a complete copper substitution of β-TCP, chemically speaking – has its own triclinic $P\bar{1}$ structure [53]. The Cu-rich HAp phase is formed during cooling by the transformation of both α-TCP and $Cu_3(PO_4)_2$ phases. XANES observations, confirmed by XPS analyses, showed the presence of mixed Cu^+/Cu^{2+} valence in samples heat-treated at 1100°C and above (Figure 6). The Cu-rich HAp phase contains both Cu^{2+} and Cu^+ cations, and the $Ca_{10}Cu_x(PO_4)_6(OH)_{2-2x}O_{2x}$ general formula used does not reflect the real copper electronic state; to be exact, it should be written $Ca_{10}Cu^{2+}_xCu^+_y(PO_4)_6(OH)_{2-2x-y}O_{2x+y}$. The refined compositions indicated in Table SEI1 consider only the presence of Cu^{2+} cation. XPS analyses determined a y/x ratio of 0.2 for the Cu-rich HAp phase in the 75Cu-1200 sample, leading to the composition $Ca_{10}Cu^{2+}_{0.51}Cu^+_{0.10}(PO_4)_6(OH)_{0.88}O_{1.12}$. Nevertheless we should remember that XPS is strictly a surface technique, with the possibility that the bulk y/x ratio can differ from the experimental 0.2 value. The mixed valence in Cu-doped HAp was already brought to light in a previous study thanks to magnetic susceptibility measurements without the quantification of the Cu^+/Cu^{2+} ratio [37]. In the case of Cu-doped belovite, larger quantities of copper cations are inserted in the apatite hexagonal channel $Sr_{10}Cu_{1.70}(PO_4)_6O_2H_y$ with exclusively the Cu^+ electronic state for a sample annealed in argon atmosphere [39,63]. The authors attributed the presence of Cu^+ to its preference for the linear coordination compared to Cu^{2+}.

As clearly reported in the review of Jin et al. [21], the benefits of using Cu-doping in the development of biomaterial applications have attracted more and more attention in recent years, despite the fact that Cu has long been considered as toxic (when its amount exceeds certain limitations). Copper is not only an essential trace element required for human body health but it presents interesting antibacterial performances, stimulates angiogenesis, and promotes osteogenesis and the inhibition of in-stent restenosis [20,21,33,64,65]. The development of Cu-containing biomaterials with better bio-adaptation must now involve a better understanding of

the cytotoxicity caused by the release of copper ions in physiological fluid: the dose-dependent cytotoxicity of copper [20]. We had in this study a complete set of materials to evaluate the cytotoxicity of the copper dopant with variations in 1) the HAp/β-TCP ratio, which impacts the copper release kinetic due to the difference in solubility between the two phases, 2) the amount of incorporated copper, which impacts the level of copper release, and 3) the copper valence (Cu^{+} and Cu^{2+}), which should impact biological behavior. First, it is essential to carry out a post-treatment on BCP sintered disks in order to suppress the high toxicity of the as-prepared samples (Figure 8a). Post-treatment is simply a washing of the disks with water, which can be combined with DMEM washing. The efficiency of these post-treatments is easily explained by the mineralogical characterization and copper location in the ceramic. The combination of the presence of free CaO (basic oxide, Table 1) and readily-available Cu^{2+} cations (either from the CuO phase for sintering at 600°C, or substituted in the soluble β-TCP for sintering at 900°C) explains the poor results in terms of cytotoxicity for disks pressed from as-synthesized BCP powder. The washing post-treatments enable the free basic CaO phase to be removed (by aqueous solubilisation) and also limit the level of copper physiological release (by a previous release in DMEM). Figure 7 evidences an almost instantaneous copper release that exceeds 10 ppm for the copper-doped samples and reaches up to 50 ppm in three weeks. Wang et al. [20] determined a critical biological level of Cu^{2+} at 10 ppm. The disk washing post-treatment enables the release level to be reduced to below 10 ppm: about 3 ppm for 600°C sintering, about 7 ppm for 900°C sintering and below 1 ppm for 1200°C sintering. These results highlight the difference in phase solubility between the known soluble β-TCP (which is mainly present in the case of 900°C sintering) and the known low-solubility HAp (single doped-HAp phase samples obtained with 1200°C sintering). On the other hand, the presence of mixed valence Cu^{+}/Cu^{2+} in the low soluble HAp phase does not penalize cell viability. As shown in Figure 8b, the best cell viabilities (above or close to the expected 100%) have been measured for the 1200°C sintering temperature; i.e. when the mixed valence is formed (Figure 6). Finally, our

MEB observations showed the biocompatibility with bone marrow cells; good adherence was highlighted with Cu-doped BCP samples (Figure 9).

6- Conclusion

The present study detailed the phase composition, the copper location and the copper electronic state of a total of 36 Cu-doped BCP samples. The temperature-dependent copper incorporation mechanism was thoroughly described. The first step (at 500°C) lead to CuO mixed with weakly-doped HAp (Cu-poor HAp). The second step, between 700°C and 1000°C, corresponds to the formation of a Cu-doped β-TCP phase mixed with the Cu-poor HAp. Finally, at 1100°C and above, samples are mainly composed of the Cu-doped HAp phase $Ca_{10}Cu_{0.6}(PO_4)_6(OH)_{0.8}O_{1.2}$ (the Cu-rich HAp). The main features of the HAp copper doping are: 1) a low amount of metal insertion for temperatures below 1100°C in Cu-poor HAP $Ca_{10}Cu_{0.1}(PO_4)_6(OH)_{1.8}O_{0.2}$, and a higher amount for temperatures above 1100°C in Cu-rich HAP $Ca_{10}Cu_{0.6}(PO_4)_6(OH)_{0.8}O_{1.2}$; 2) the necessity to decompose high-temperature Cu-doped α-TCP polymorph and $Cu_3(PO_4)_2$ to form the Cu-rich HAp phase; and 3) the presence of the mixed Cu^+/Cu^{2+} valence. Amongst our set of copper-doped BCP samples, we have several promising bioceramics for bone substitution and/or prosthesis coating. A mixture of HAp and β-TCP phases is interesting because of their difference in solubility; mixing Cu-doped HAp and β-TCP phases enables the copper releasing kinetics to be regulated. And the presence of Cu^+ cations in samples heat-treated at 1100°C and above is potentially interesting for biomaterial applications. The ionic releases from sintered disks obtained from pressed BCP powder were observed, in order to establish a post-treatment to obtain acceptable or even very good cytotoxicity values. An understanding of the biological behavior (here in terms of cytotoxicity) and the mastery of BCP bioceramic preparation are only possible because the BCP doping mechanism has been clearly identified beforehand.

Acknowledgements

This work was supported by ANR under project NANOSHAP (ANR-09-BLAN-0120-03) and the CNRS 2015 PEPS project. We gratefully acknowledge SLS for the provision of synchrotron radiation facilities and we would like to thank Maarten Nachtegaal for his assistance in using the SuperXAS beamline.

References

[1] S. V. Dorozhkin, *Biomater.*, Biocomposites and hybrid biomaterials based on calcium orthophosphates, 1 (2011) 3-56.

[2] S. G. Dahl, P. Allain, P. J. Marie, Y. Mauras, G. Boivin, P. Ammann, Y. Tsouderos, P. D. Delmas and C. Christiansen, *Bone*, Incorporation and distribution of strontium in bone, 28 **(**2001) 446–453.

[3] R. Lagier and C. A. Baud, *Pathol. Res. Pract.*, Magnesium whitlockite, a calcium phosphate crystal of special interest in pathology, 199 (2003) 329–335.

[4] R. S. Lee, M. V. Kayser and S. Y. Ali, *J. Anat.*, Calcium phosphate microcrystal deposition in the human intervertebral disc, 208 (2006) 13–19.

[5] C. Rey, C. Combes, C. Drouet and M. J. Glimcher, *Osteoporos Int.*, Bone mineral: update on chemical composition and structure, 20 (2009) 1013-1021.

[6] S. Cazalbou, C. Combes, D. Eichert and C. Rey, *J. Mater. Chem.*, Adaptative physico-*chemistry* of bio-related calcium phosphates, 14 (2004) 2148-2153.

[7] J. C. Elliot, Structure and chemistry of the apatite and other calcium orthophosphates, Amsterdam: Elsevier, 1994.

[8] S. Gomes, J.-M. Nedelec, E. Jallot, D. Sheptyakov and G. Renaudin, *Chem. Mater.*, Structural characterization and biological fluid interaction of solgel-derived Mg-substituted biphasic calcium phosphate ceramics, 23 (2011) 3072-3085.

[9] S. Gomes, J.-M Nedelec and G. Renaudin, *Acta Biomater.*, On the effect of temperature on the insertion of zinc into hydroxyapatite, 8 (2012) 1180-1189.

[10] S. Gomes, A. Kaur, J.-M Nedelec and G. Renaudin, *J. Mater. Chem. B*, X-ray Absorption Spectroscopy shining (synchrotron) light onto the insertion of Zn^{2+} in calcium phosphate ceramics and its influence on their behaviour in biological conditions, 2 (2014) 536-545.

[11] S. Gomes, A. Kaur, J.-M. Grenèche, J.-M. Nedelec and G. Renaudin, *Acta Biomater.*, Atomic scale modeling of iron-doped biphasic calcium phosphate bioceramics, 50 (2017) 78-88.

[12] G. Renaudin, S. Gomes and J.-M. Nedelec, *Materials*, First-row transition metal doping in calcium phosphate bioceramics: a detailed crystallographic study, **10 (**2017) 92-113.

[13] Z. Radovanovic, B. Jokic, D. Veljovic, S. Dimitrijevic, V. Kojic, R. Petrovic and D. Janackovic, *Appl. Surf. Sci.*, Antimicrobial activity and biocompatibility of Ag^{+}- and Cu^{2+}-doped biphasic hydroxyapatite/α-tricalcium phosphate obtained from hydrothermally synthesized Ag^{+}- and Cu^{2+}-doped hydroxyapatite, 307 (2014) 513-519.

[14] D. H. Nies, *Appl. Microbiol. Biotechnol*, Microbial heavy-metal resistance, 51 (1999) 730-750.

[15] H. G. Petering, *Pharmacol. Ther. A*, Pharmacology and toxicology of heavy metals: Silver, 1 (1976) 127-130.

[16] W. J. Schreurs and H. Rosenberg, *J. Bacteriol.*, Effect of silver ions on transport and retention of phosphate by Escherichia coli, 152 (1982) 7-13.

[17] R. O. Darouiche, *Clin. Infect. Dis.*, Anti-infective efficacy of silver-coated medical prostheses, 29 (1999) 1371-1377.

[18] G. Borkow and J. Gabbay, *Curr. Med. Chem.*, Copper as a biocidal tool, 12 (2005) 2163-2175.

[19] Q. L. Feng, J. Wu, G. Q. Chen, F. Z. Cui, T. N. Kim and J. O. Kim, *J. Biomed. Mater. Res.*, A mechanistic study of the antibacterial effect of silver ions on Escherichia coli and Staphylococcus aureus, 52 (2000) 662-668.

[20] X. Wang, F. Cheng, J. Liu, J.-H. Smatt, D. Gepperth, M. Lastusaari, C. Xu and L. Hupa, *Acta Biomaterialia*, Biocomposites of copper-containing mesoporous bioactive glass and nanofibrillated cellulose: Biocompatibility and angiogenic promotion in chronic wound healing application, 46 (2016) 286-298.

[21] S. Jin, L. Ren and K. Yang, *J. Mater. Sci. Tech.*, Bio-functional Cu containing biomaterials: a new way to enhance bio-adaption of biomaterials, 32 (2016) 835-839.

[22] B. R. Stern, *J. Toxicol. Environ. Health Part A*, Essentiality and Toxicity in Copper Health Risk Assessment: Overview, Update and Regulatory Considerations, 73 (2010) 114-127.

[23] M. Hunt, *Curr. Opin. Orthop.*, Copper and boron as examples of dietary trace elements important in bone development and disease, 9 (1998) 28-36.

[24] H. Opsahl, Zeroniam, M. Ellison, D. Lewis, R. B. Rucker and R. S. Riggins, *J. Nutr.*, Role of copper in collagen cross-linking and its influence on selected mechanical properties of chick bone and tendon, 112 (1982) 708-716.

[25] N. M. Lowe, W. D. Fraser and M. J. Jackson, *Proc. Nutr. Soc.*, Is there a potential therapeutic value of copper and zinc for osteoporosis?, 61 (2002) 181-185.

[26] C. Wu, Y. Zhou, M. Xu, P. Han, L. Chen, J. Chang and Y. Xiao, *Biomater.*, Copper-containing mesoporous bioactive glass scaffolds with multifunctional properties of angiogenesis capacity, osteostimulation and antibacterial activity, 34 (2013) 422-433.

[27] E. A. Neel, I. Ahmed, J. Prattern, S. N. Nazhat and J. C. Knowles, *Biomater.*, Characterisation of antibacterial copper releasing degradable phosphate glass fibres, 26 (2005) 2247-2254.

[28] S. Jaiswal, P. McHale and P. Duffy, *Collloids Surf B Biointerfaces*, Preparation and rapid analysis of antibacterial silver, copper and zinc doped sol–gel surfaces, 94 (2012) 170-176.

[29] G. F. Hu, *J. Cell. Biochem.*, Copper stimulates proliferation of human endothelial cells under culture, 69 (1998) 326-335.

[30] C. K. Sen, S. Khanna, M. Venojarvi, P. Trikha, E. C. Ellison and T. K. Hunt, *Am. J. Physiol Heart Circ. Physiol.*, Copper-induced vascular endothelial growth factor expression and wound healing, 282 (2002) H1821-1827.

[31] M. Frangoulis, P. Georgiou, C. Chrisostomidis, D. Perrea, I. Dontas and N. Kavantzas, *Plast. Reconstr. Surg.*, Rat Epigastric Flap Survival and VEGF Expression after Local Copper Application, 119 (2007) 837-843.

[32] A. Ewald, C. Kappel, E. Vorndran, C. Moseke, M. Gelinsky and U. Gbureck, *J. Biomed. Mater. Res. Part A*, The effect of Cu(II)-loaded brushite scaffolds on growth and activity of osteoblastic cells, 100 (2012) 2392-2400.

[33] R. A. Popescu, K. Magyari, A. Vulpoi, D. L. Trandafir, E. Licarete, M. Todea, R. Stefan, C. Voica, D. C. Vodnar, S. Simon, I. Papuc and L. Baia, *Biomater. Sci.*, Bioactive and biocompatible copper containing glass-ceramics with remarkable antibacterial properties and high cell viability designed for future *in vivo* trials, 4 (2016) 1252-1265.

[34] M. Pujari and P. N. Patel, *J. Solid State Chem.*, Strontium-copper-calcium hydroxyapatite solid solutions: Preparation, infrared, and lattice constant measurements, 83 (1989) 100-104.

[35] N. K. Triphathy, P. N. Patel and A. Panda, *J. Solid State Chem.*, Preparation, IR, and lattice constant measurements of mixed (Ca + Cu + Zn) hydroxylapatites, 80 (1989) 1-5.

[36] S. Shanmugam and B. Gopal, *Ceram. Int.*, Copper substituted hydroxyapatite and fluorapatite: Synthesis, characterization and antimicrobial properties, 40 (2014) 15655-15662.

[37] A. S. Karpov, J. Nuss, M. Jansen, P. E. Kazin and Y. D. Tretyakov, *Solid State Sci*., Synthesis, crystal structure and properties of calcium and barium hydroxyapatites containing copper ions in hexagonal channels, 5 (2003) 1277–1283.

[38] T. Baikie, G. M. H. Ng, S. Madhavi, S. P. Pramana, K. Blake, M. Elcombe and T. J. White, *Dalton Trans.*, The crystal chemistry of the alkaline-earth apatites $A_{10}(PO_4)_6Cu_xO_y(H)_z$ (A = Ca, Sr and Ba), 34 (2009) 6722-6726.

[39] F. E. Imrie, J. M. S. Skakle and I. R. Gibson, *Bioceram. Dev. Appl.*, Preparation of Copper-Doped Hydroxyapatite with Varying x in the Composition $Ca_{10}(PO_4)_6Cu_xO_yH_z$, (2013) S1:005, doi: 10.4172/2090-5025.S1-005

[40] J. Rodriguez-Carvajal, PROGRA*M FullProf.2k* – version 3.20; Laboratoire Léon Brillouin (CEA-CNRS): Saclay, France, 2005; FullProf.2k manual available on http://www-llb.cea.fr/fullweb/fp2k/fp2k_divers.htm. See also J. Rodriguez-Carvajal, T. Roisnel, *EPDIC-8;* May 23-26, 2002; Trans. Tech. Publication: Uppsala, Sweden; Mater. Sci. Forum 2004; 123:443.

[41] N. Newville, *J. Synchrotron Rad.*, IFEFFIT : interactive XAFS analysis and FEFF fitting, 8 (2001) 322-324.

[42] B. Ravel, *J. Synchrotron Rad.*, ATOMS: crystallography for the X-ray absorption spectroscopist, 8 (2001) 314-316.

[43] J. J. Rehr, J. Mustre de Leon, S. I. Zabinsky and R. C. Albers, *J Am Chem Soc*, Theoretical x-ray absorption fine structure standards, 113 (1991) 5135-5145.

[44] D. Shirley, *Phys. Rev. B*, High-Resolution X-Ray Photoemission Spectrum of the Valence Bands of Gold, 5 (1972) 4709–4714.

[45] J. Scofield, *J. Electron Spectrosc. Relat. Phenom.*, Hartree-Slater subshell photoionization cross-sections at 1254 and 1487 eV, 8 (1976) 129–137.

[46] G. Renaudin, P. Laquerrière, Y. Filinchuk, E. Jallot and J.-M. Nedelec, *J. Mater. Chem.*, Structural characterization of sol–gel derived Sr-substituted calcium phosphates with anti-osteoporotic and anti-inflammatory properties, 18 (2008) 3593-3600.

[47] G. Renaudin, E. Jallot and J.-M. Nedelec, *J. Sol-Gel Sci. Technol.*, Effect of strontium substitution on the composition and microstructure of sol-gel derived calcium phosphate, 51 (2009) 287-294.

[48] S. Gomes, G. Renaudin, E. Jallot and J.-M. Nedelec, *Appl. Mater. Interfaces*, Structural characterization and biological fluid interaction of sol-gel derived Mg-substituted biphasic calcium phosphate ceramics, 1 (2009) 505-513.

[49] L. M. Rodriguez-Lorenzo, J. N. Hart and A. Gross, *J. Phys. Chem. B*, Structural and Chemical Analysis of Well-Crystallized Hydroxyfluorapatites, 107 (2003) 8316–8320.

[50] M. Yashima, A. Sakai, T. Kamiyama and A. Hoshikawa, *J. Solid State Chem.*, Crystal structure analysis of β-tricalcium phosphate $Ca_3(PO_4)_2$ by neutron powder diffraction, 175 (2003) 272–277.

[51] B. I. Lazoryak, N. Khan, V. A. Morozov, A. A. Belik and S. S. Khasanov, *J. Solid State Chem.*, Preparation, structure determination, and redox characteristics of new calcium copper phosphates, 145 (1999) 345-355.

[52] V. Yu. Pomjakushin, A. Furrer, D. V. Sheptyakov, E. V. Pomjakushina and K. Conder, Phys. Rev. B, Crystal and magnetic structures of the spin-trimer compounds $Ca_3Cu_{3-x}Ni_x(PO_4)_4$ (x=0,1,2), 76 (2007) 174433-174439.

[53] G. L. Shoemaker, J. B. Anderson and E. Kostiner, *Acta Crystallogr. Sect. B: Sturct. Sci*, Copper(II) phosphate, 33 (1977) 2969-2972.

[54] S. P. Cramer and K. O. Hodgson, *Prog. Inorg. Chem.*, X-ray absorption spectroscopy: a new structural method and its applications to bioinorganic chemistry, 25 (1979) 1-39.

[55] P. A. Lee, P. H. Citrin, P. Eisenberger, B. M. Kincaid, *Rev. Mod. Phys.*, Extended x-ray absorption fine structure—its strengths and limitations as a structural tool, 53 (1981) 769-806.

[56] E. I. Solomon, In *Comments of Inorganic Chemistry;* Sutin, Norman, Ed.; Gordon & Breach: New York, 1984; Vol. 3, pp 225-320.

[57] L.S Kau, D.J. Spria-Solomon, J.E. Penner-Hahn, K.O. Hodgson and E.I. Solomon, *J. Am. Chem. Soc.*, X-ray absorption edge determination of the oxidation state and coordination number of copper. Application to the type 3 site in Rhus vernicifera laccase and its reaction with oxygen, 109 (1987) 6433-6442.

[58] A. Gaur, B. D. Shrivastava and S. K. Joshi, 14th International Conference on X-Ray Absorption Fine Structure (XAF14) journal of Physics: Conference series 190, 2009, 012084.

[59] L. Martin, H. Martinez, D. Poinot, B. Pecquenard and F. Le Cras, *J. Phys. Chem. C*, Comprehensive X-ray photoelectron spectroscopy study of the conversion reaction mechanism of CuO in lithiated thin film electrodes, 117 (2013) 4421–4430.

[60] S. Harmer, W. Skinner, A. Buckley, and L.-J. Fan, *Surf.* Sci., Species formed at cuprite fracture surfaces; observation of O 1s surface core level shift, 603 (2009) 537–545.

[61] F. Parmigiani, L. Depero, T. Minerva, and J. Torrance, *J. Electron Spectrosc. Relat. Phenom.*, The fine structure of the Cu $2p_{3/2}$ X-ray photoelectron spectra of copper oxide based compounds, 58 (1992) 315–323.

[62] F. Parmigiani, G. Pacchioni, F. Illas, and P. Bagus, *J. Electron Spectrosc. Relat. Phenom.*, Studies of the Cu-O bond in cupric oxide by X-ray photoelectron spectroscopy and ab initio electronic structure models, 59 (1992) 255–269.

[63] P. E. Kazin, A. S. Karpov, J. Martin, J. Nuss and Y. D. Tretyakov, *Z. Anorg. Allg. Chem.*, Crystal structure and properties of strontium phosphate apatite with oxocuprate ions in hexagonal channels, 629 (2003) 344-3520.

[64] V. Stanic, S. Dimitrijevic, J. A. Stankovic, M. Mitric, B. Jokic, I. B. Plecas and S. Raicevic, *Appl. Surf. Sci.*, Synthesis, characterization and antimicrobial activity of copper and zinc-doped hydroxyapatite nanopowders, 256 (2010) 6083-6089.

[65] N. Matsumoto, K. Sato, K. Yoshida, K. Hashimoto and Y. Toda, *Acta Biomater.*, Preparation and characterization of β-tricalcium phosphate co-doped with monovalent and divalent antibacterial metal ions, 5 (2009) 3157-3164.

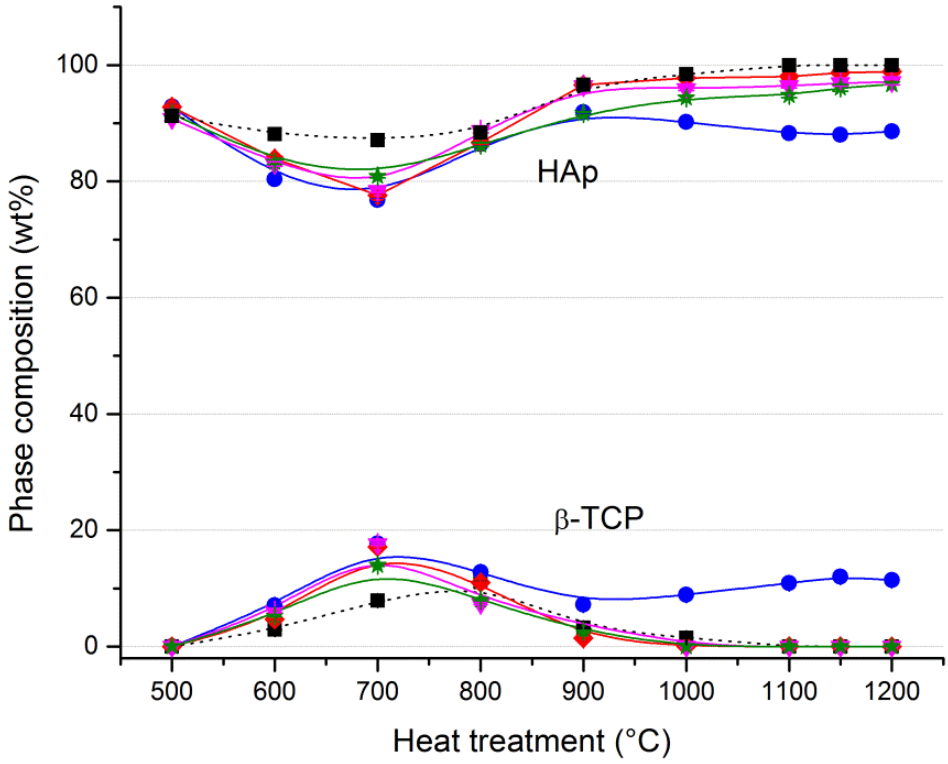

Figure 1. Mineral composition of the two main phases (HAp and β-TCP) as a function of sintering temperature for the five series: undoped (black squares, dotted lines), 15Cu-T (blue circles, solid lines), 25Cu-T (red diamonds, solid lines), 50Cu-T (pink triangles, solid lines) and 75Cu-T (green stars, solid lines).

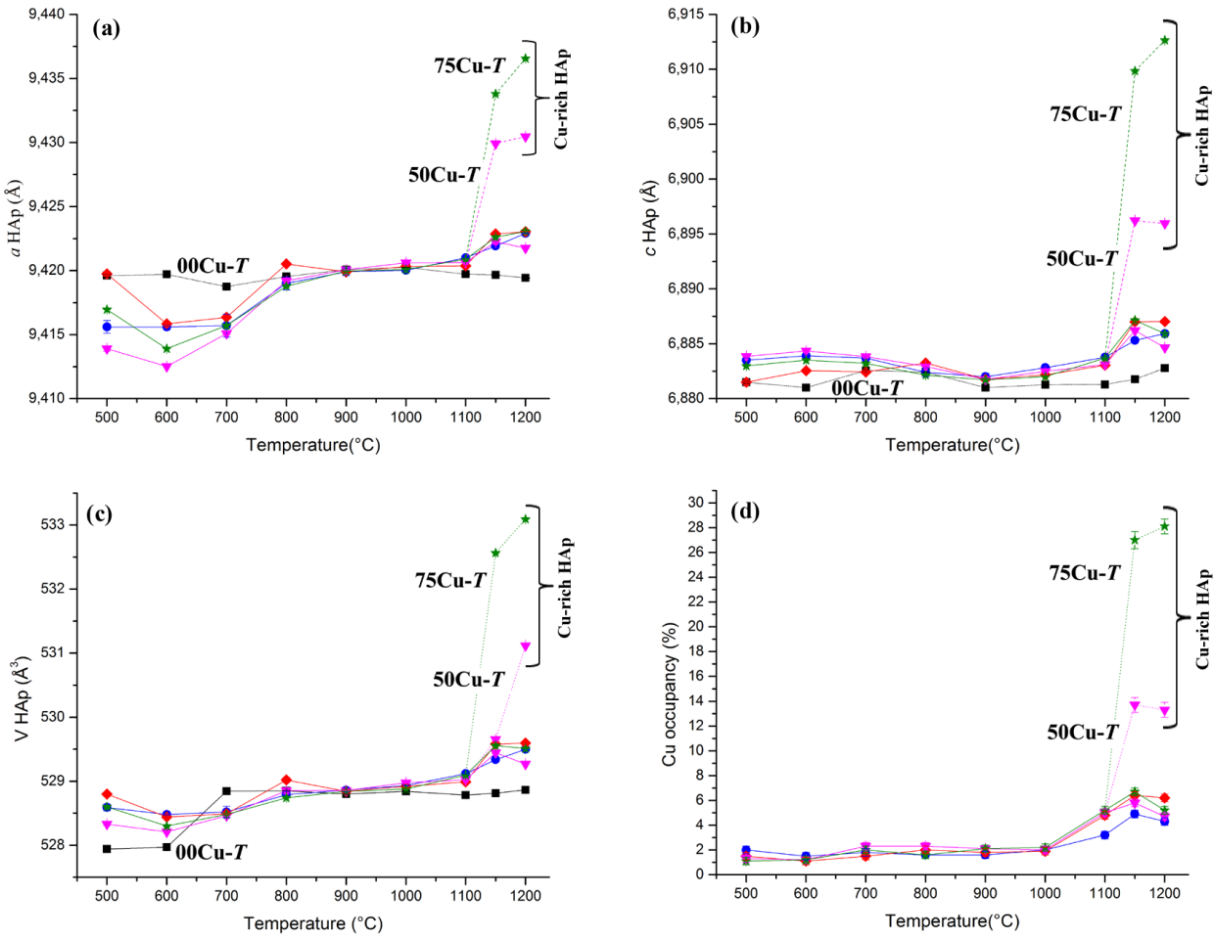

Figure 2. Thermal variations in HAp lattice parameters: **(a)** lattice parameters a, **(b)** lattice parameter c, **(c)** unit cell volume, and **(d)** the Cu occupancy factor attributed to the 2b Wyckoff site (0,0,0). The undoped series 00Cu-T (black squares), and the Cu-doped series 15Cu-T (blue circles), 25Cu-T (red diamonds), 50Cu-T (pink triangles and 75Cu-T (green stars) are represented. Solid lines correspond to variation in the undoped and Cu-poor HAp (i.e. HAp1 in Tables 1 and 2) phases, whereas dotted lines correspond to the Cu-rich HAp (i.e. HAp2 in Tables 1 and 2) phase resolved in the two 50Cu-T and 75Cu-T series.

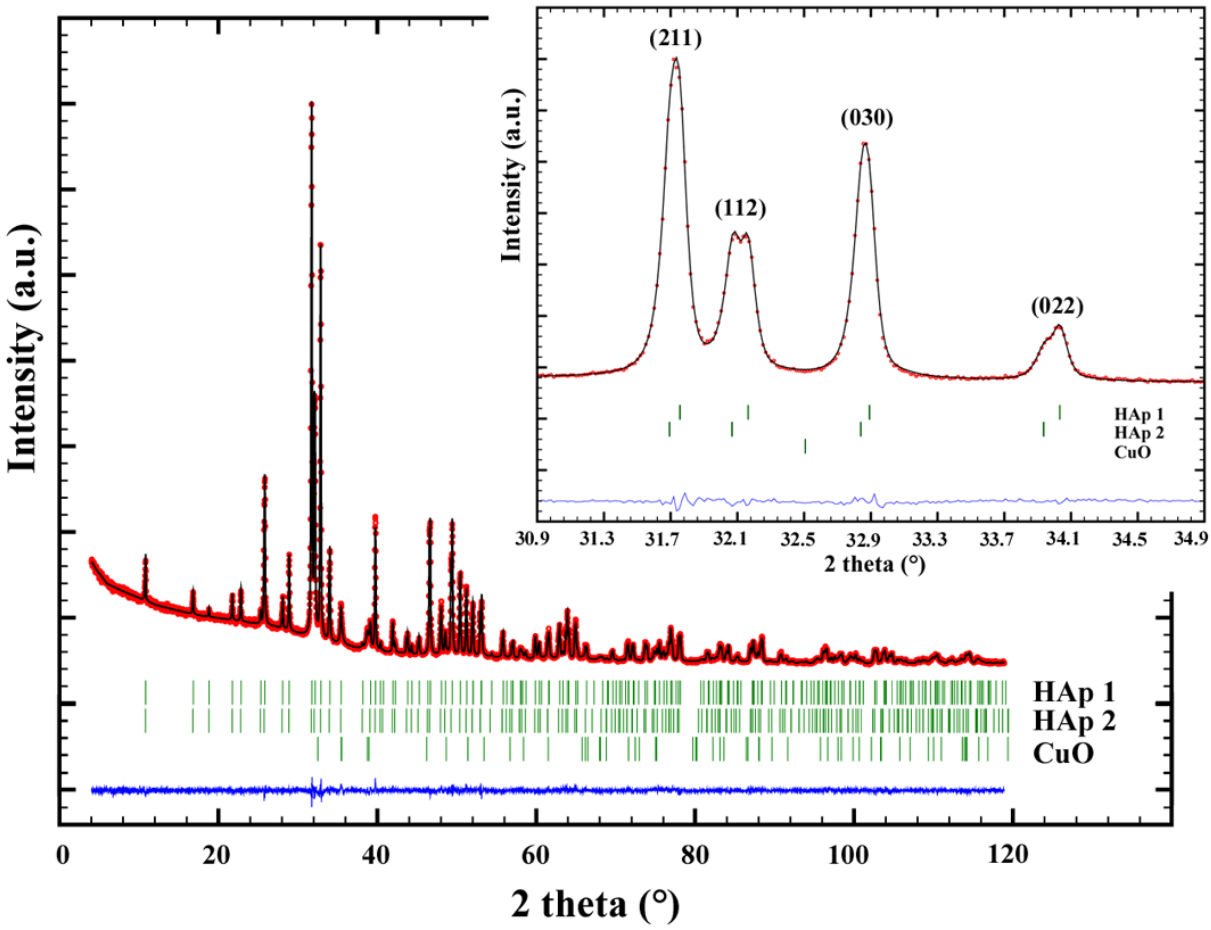

Figure 3. Rietveld refinement performed on 75Cu-1200 pattern recorded in transmission mode, showing the presence of two HAp phases: HAp1 for the Cu-poor HAp phase and HAp2 for the Cu-rich HAp phase. Inset shows the 2-theta resolution conveyed by transmission geometry.

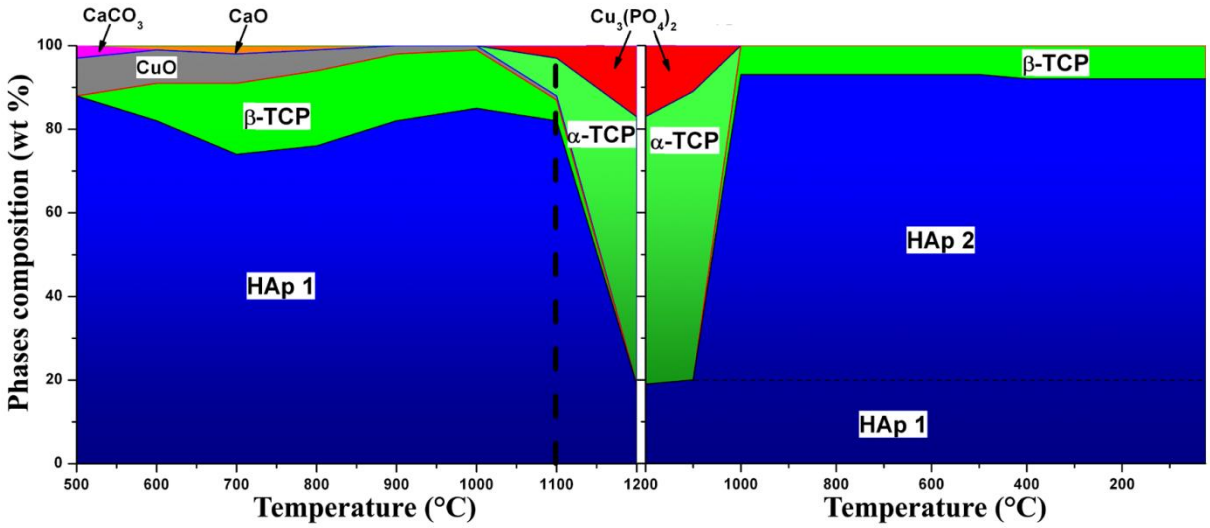

Figure 4. Temperature phase evolution extracted from Rietveld refinements performed on in-situ XRPD measurements using a HTK chamber on the 75Cu-*T* series.

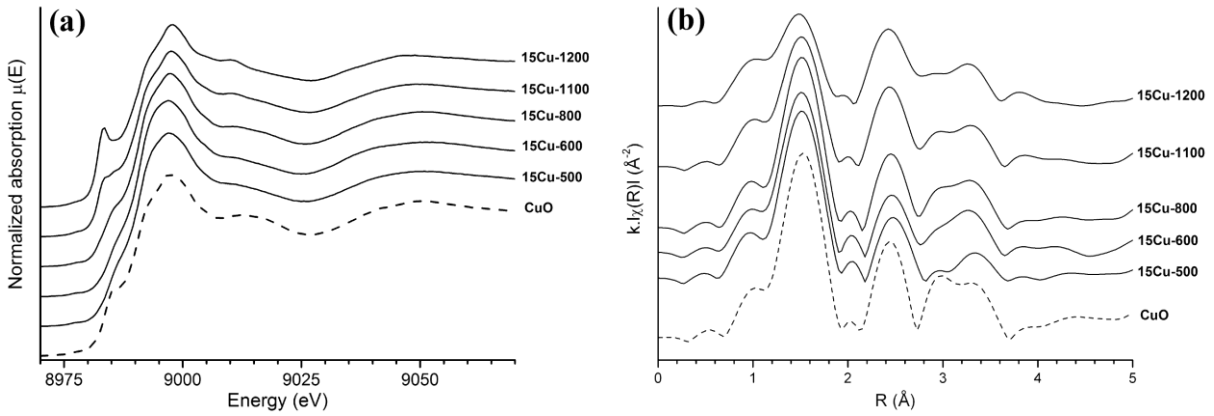

Figure 5. (a) XANES part of the XAS spectra, and (b) k-weighted amplitudes of the Fourier transform, uncorrected for phase shift, for the 15Cu-T series samples (solid lines) and the reference compound (CuO, dashed lines).

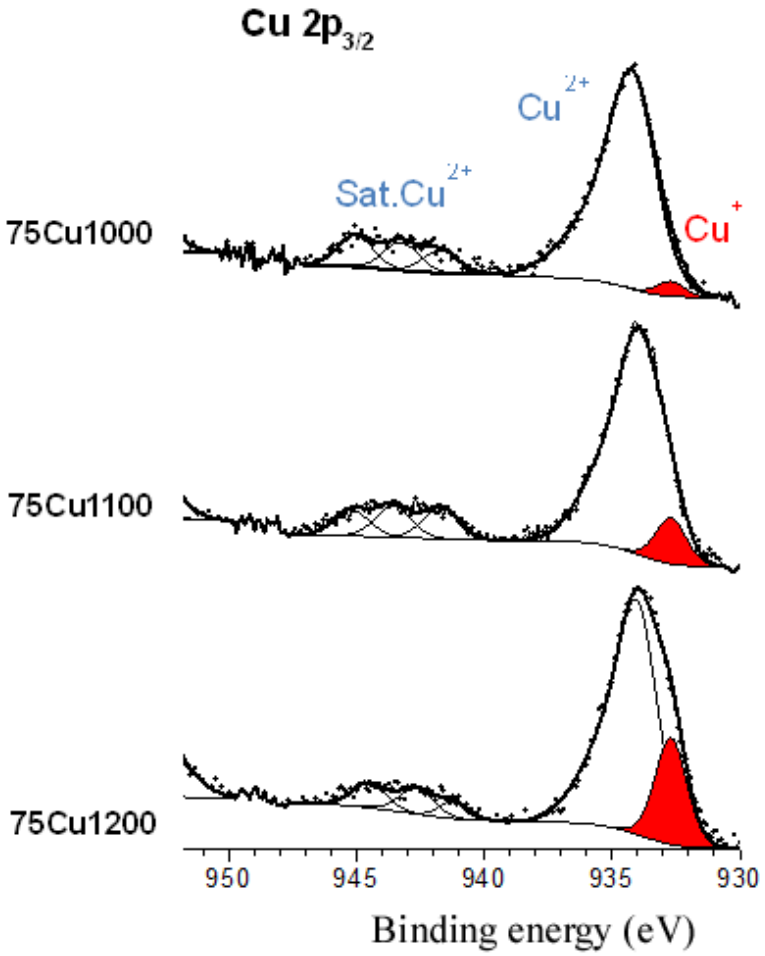

Figure 6. Cu $2p_{3/2}$ XPS core peak of three samples from the 75Cu-T series (from 1000°C to 1200°C).

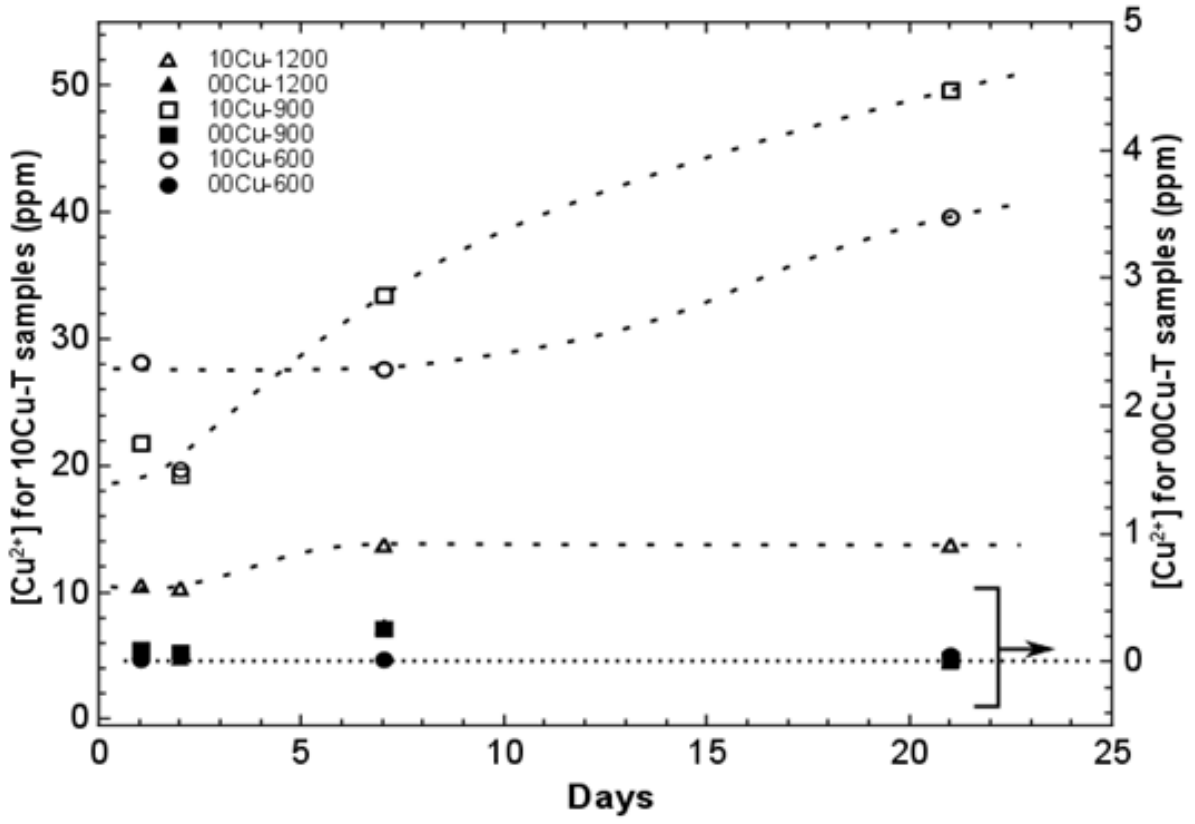

Figure 7. Copper ion concentration in DMEM versus disk immersion time at 37°C for undoped and 10Cu-T samples annealed at 600, 900 and 1200°C.

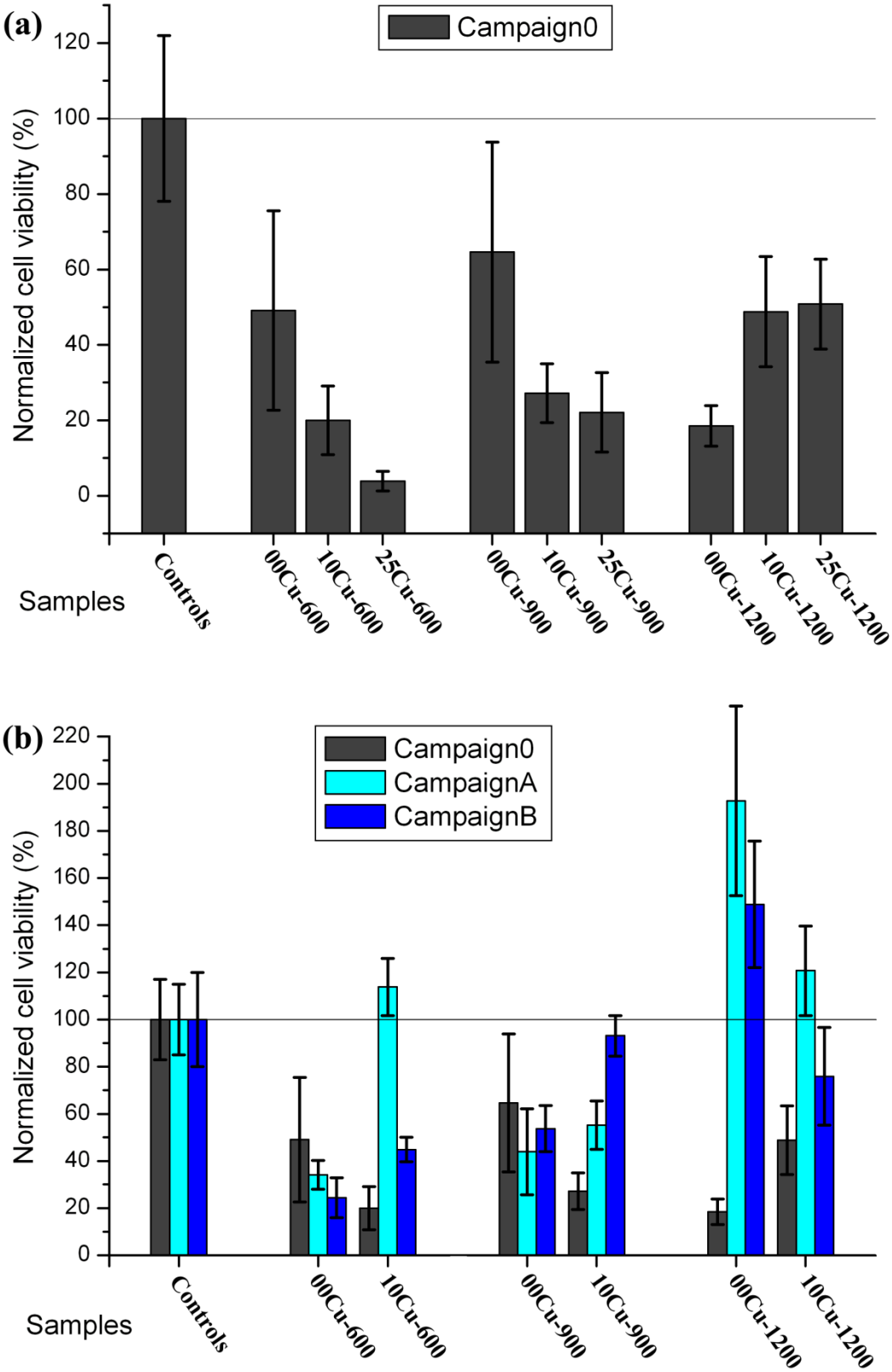

Figure 8. Cell viability evaluation for a) Series 0 for xCu-T samples with x = 00, 10 and 20; and b) with Series A and B for xCu-T samples with x = 00 and 10. Error bars represent the standard error of mean from triplicate samples.

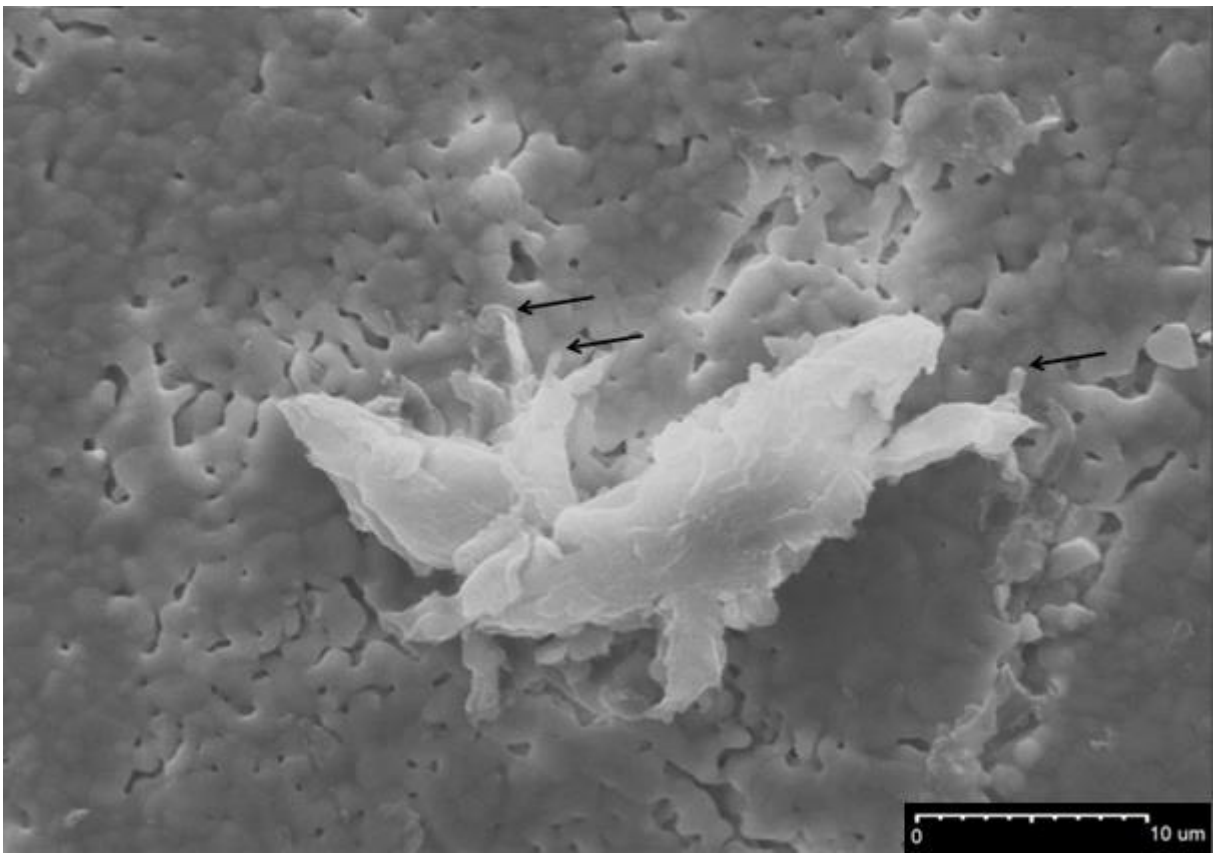

Figure 9. Bone marrow adherent cell after 8 days of culture on a 10Cu-600 ceramic disk. These cells develop a strong attachment to the material surface through cellular expansion (black arrows).

Table 1. Results of quantitative analyses (wt %) extracted from Rietveld refinements for the undoped BCP series and the Cu-doped BCP series. Standard deviations are indicated in parentheses.

Samples	Mineralogical composition (wt %)						
	HAp1	HAp2	β-TCP	α-CDP	$CaCO_3$	CaO	CuO
00Cu-500	91.2 (9)	-	-	4.4 (3)	3.7 (2)	0.8 (1)	-
00Cu-600	88.1 (9)	-	2.9 (3)	7.2 (3)	0.9 (1)	1.0 (1)	-
00Cu-700	87.1 (9)	-	7.9 (3)	3.9 (3)	0.5 (1)	0.6 (1)	-
00Cu-800	88.4 (9)	-	11.1 (3)	-	-	0.5 (1)	-
00Cu-900	96.6 (6)	-	3.2 (3)	-	-	0.2 (1)	-
00Cu-1000	98.4 (9)	-	1.5 (3)	-	-	0.1 (1)	-
00Cu-1100	100 (-)	-	-	-	-	-	-
00Cu-1150	100 (-)	-	-	-	-	-	-
00Cu-1200	100 (-)	-	-	-	-	-	-
10Cu-600	88.5 (9)	-	2.4 (4)	6.2 (4)	1.1 (1)	1.8 (1)	-
10Cu-900	94.2 (8)	-	5.8 (4)	-	-	-	-
10Cu-1200	98.6 (5)	-	1.4 (3)	-	-	-	-
15Cu-500	92.9 (4)	-	-	2.9 (1)	3.1 (1)	0.5 (1)	0.6 (1)
15Cu-600	80.4 (4)	-	7.1 (2)	9.2 (2)	1.3 (2)	1.0 (1)	1.0 (1)
15Cu-700	76.8 (3)	-	17.7 (2)	3.4 (1)	0.8 (1)	0.9 (1)	0.3 (1)
15Cu-800	86.4 (3)	-	12.8 (1)	-	-	-	0.9 (1)
15Cu-900	91.9 (3)	-	7.2 (1)	-	-	-	0.9 (1)
15Cu-1000	90.2 (3)	-	8.9 (9)	-	-	-	0.9 (1)
15Cu-1100	88.3 (3)	-	10.9 (1)	-	-	-	0.8 (1)
15Cu-1150	88.0 (3)	-	12.0 (1)	-	-	-	-
15Cu-1200	88.6 (3)	-	11.4 (1)	-	-	-	-
		-	-				
25Cu-500	92.8 (4)	-	-	2.4 (1)	2.5 (1)	1.3 (1)	1.0 (1)
25Cu-600	83.9 (4)	-	4.7 (1)	8.5 (2)	0.3 (1)	1.5 (1)	1.0 (1)
25Cu-700	77.6 (3)	-	17.1 (2)	2.4 (1)	-	1.7 (1)	1.0 (1)
25Cu-800	86.7 (3)	-	11.0 (1)	-	-	0.5 (1)	1.8 (1)
25Cu-900	96.6 (3)	-	1.4 (7)	-	-	-	2.0 (1)
25Cu-1000	97.8 (3)	-	-	-	-	-	2.2 (1)
25Cu-1100	98.1 (4)	-	-	-	-	-	1.9 (1)
25Cu-1150	98.7 (4)	-	-	-	-	-	1.3 (1)
25Cu-1200	98.9 (4)	-	-	-	-	-	1.1 (1)
		-					
50Cu-500	90.8 (4)	-	-	2.3 (1)	2.5 (1)	0.8 (1)	2.9 (1)
50Cu-600	83.0 (4)	-	6.0 (2)	6.9 (1)	-	1.4 (1)	2.7 (1)
50Zn-700	78.4 (3)	-	17.6 (2)	-	-	1.2 (1)	2.8 (1)
50Cu-800	88.7 (3)	-	7.4 (2)	-	-	0.4 (1)	3.5 (1)
50Cu-900	96.4 (3)	-	-	-	-	-	3.6 (1)
50Cu-1000	96.2 (3)	-	-	-	-	-	3.8 (1)
50Cu-1100	96.6 (3)	-	-	-	-	-	3.4 (1)
50Cu1150	67.8 (4)	29.1 (3)	-	-	-	-	2.8 (1)
50Cu1200	66.5 (4)	30.6 (3)	-	-	-	-	2.7 (1)
75Cu-500	91.7 (4)	-	-	1.9 (1)	1.7 (1)	0.3 (1)	4.3 (1)
75Cu-600	83.3 (4)	-	5.3 (2)	6.3 (2)	-	0.8 (1)	4.3 (1)
75Zn-700	80.9 (3)	-	14.0 (2)	-	-	0.7 (1)	4.4 (1)
75Cu-800	86.3 (3)	-	8.0 (1)	-	-	0.2 (1)	5.4 (1)
75Cu-900	91.7 (3)	-	2.6 (2)	-	-	-	5.7 (1)
75Cu-1000	94.4 (3)	-	-	-	-	-	5.6 (1)
75Cu-1100	94.8 (4)	-	-	-	-	-	5.2 (1)
75Cu-1100*	81 (1)*	13.5 (6)*	-	-	-	-	5.1 (1)*
75Cu-1150	75.5 (5)	20.6 (3)	-	-	-	-	3.9 (1)
75Cu-1200	62.6 (4)	34.1 (3)	-	-	-	-	3.3 (1)
75Cu-1200*	58.9 (8)*	37.6 (7)*	-	-	-	-	3.5 (1)*

* Rietveld refinement results from XRPD in transmission mode measured with capillaries.

Table 2. Rietveld refinement results from XRPD patterns recorded in transmission mode on capillaries (lattice parameters a and c, unit cell volume V, atomic coordinates x, y and z, temperature factors B_{iso} and occupancies) for the two HAp phases from the 75Cu-1200 samples. Standard deviations are indicated in parentheses. $R_p = 0.11$ and $R_{wp} = 0.10$ represent conventional Rietveld agreement factors.

HAp	Atom	Site	*x*	*y*	*z*	B_{iso} (Å^2)	Occ.*
HAp1: Cu-poor HAp phase; $Ca_{10}Cu_{0.10(1)}(PO_4)_6(OH)_{1.80(2)}O_{0.20(2)}$							
*P*6$_3$/*m*	Ca1	4*f*	⅓	⅔	0.0023(4)	0.5(1)	1(-)
a = 9.42492(8) Å	Ca2	6*h*	0.2468(3)	0.9933(3)	¼	= B_{Ca1}	1(-)
c = 6.88839(6) Å	P1	6*h*	0.3992(3)	0.3684(3)	¼	0.3(1)	1(-)
V = 529.912(8) Å^3	O1	6*h*	0.3264(7)	0.4819(7)	¼	0.5(1)	1(-)
	O2	6*h*	0.5853(7)	0.4658(7)	¼	= B_{O1}	1(-)
	O3	12*i*	0.3406(4)	0.2549(5)	0.0705(5)	= B_{O1}	1(-)
	O4	4*e*	0	0	0.203(2)	= B_{O1}	½(-)
	Cu1	2*b*	0	0	0	= B_{Ca1}	0.048(6)
HAp2: Cu-rich HAp phase; $Ca_{10}Cu_{0.61(1)}(PO_4)_6(OH)_{0.78(2)}O_{1.22(2)}$							
*P*6$_3$/*m*	Ca1	4*f*	⅓	⅔	0.0018(7)	0.5(1)	1(-)
a = 9.43954(9) Å	Ca2	6*h*	0.2488(4)	0.9933(4)	¼	= B_{Ca1}	1(-)
c = 6.91356(7) Å	P1	6*h*	0.3981(4)	0.3677(4)	¼	0.3(1)	1(-)
V = 533.500(9) Å^3	O1	6*h*	0.330(1)	0.486(1)	¼	0.5(1)	1(-)
	O2	6*h*	0.587(1)	0.465(1)	¼	= B_{O1}	1(-)
	O3	12*i*	0.3426(7)	0.2591(7)	0.0696(7)	= B_{O1}	1(-)
	O4	4*e*	0	0	0.209(3)	= B_{O1}	½(-)
	Cu1	2*b*	0	0	0	= B_{Ca1}	0.307(6)

* Occupancy parameters.

Supplementary Information

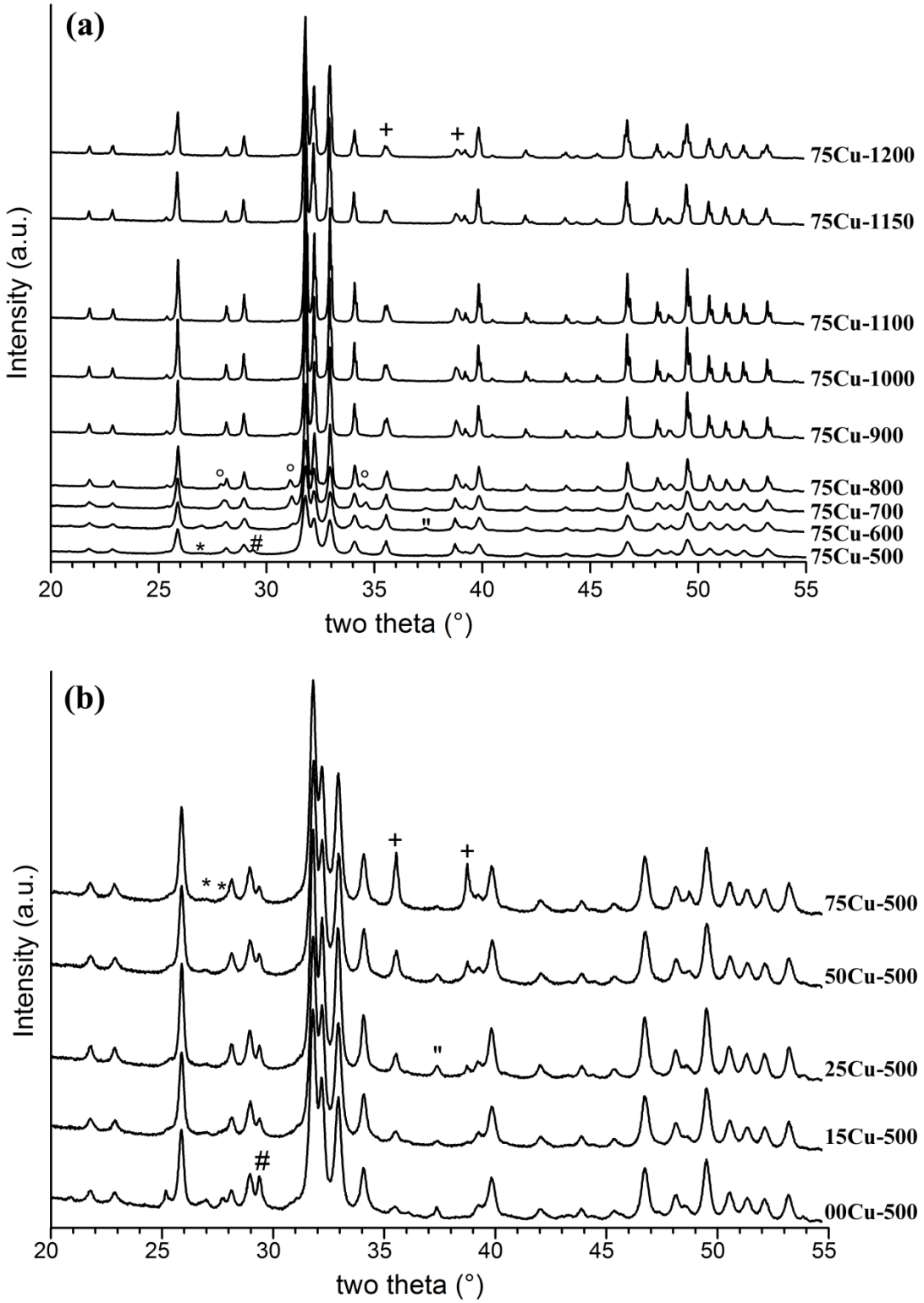

Figure SE1. Selected XRPD patterns (λ = 1.5418 Å) showing (a) the 75Cu-*T* series and (b) the *x*Cu-500 samples. Main phase is Hap for all patterns, minor phases are CuO (+), β-TCP (°), α-CDP (*), $CaCO_3$ (#) and CaO (”).

Table SEI1. Structural parameters of the HAp phase obtained by Rietveld refinements.

Samples	HAp structural parameters				
	a (Å)	*c* (Å)	V (Å^3)	Cu Occ $^{(**)}$	Refined composition
00Cu-500	9.4196 (1)	6.88419 (1)	528.94 (1)	-	$Ca_{10}(PO_4)_6(OH)_2$
00Cu-600	9.4197 (1)	6.88410 (9)	528.97 (1)	-	$Ca_{10}(PO_4)_6(OH)_2$
00Cu-700	9.41874 (9)	6.88356 (8)	528.846 (9)	-	$Ca_{10}(PO_4)_6(OH)_2$
00Cu -800	9.41954 (5)	6.88241 (4)	528.848 (5)	-	$Ca_{10}(PO_4)_6(OH)_2$
00Cu -900	9.42007 (3)	6.88100 (3)	528.799 (3)	-	$Ca_{10}(PO_4)_6(OH)_2$
00Cu -1000	9.42025 (2)	6.88127 (2)	528.840 (2)	-	$Ca_{10}(PO_4)_6(OH)_2$
00Cu -1100	9.41972 (3)	6.88129 (2)	528.782 (3)	-	$Ca_{10}(PO_4)_6(OH)_2$
00Cu -1150	9.41966 (3)	6.88177 (3)	528.812 (3)	-	$Ca_{10}(PO_4)_6(OH)_2$
00Cu -1200	9.41942 (3)	6.88278 (3)	528.863 (3)	-	$Ca_{10}(PO_4)_6(OH)_2$
15Cu -500	9,4156(5)	6,8835 (2)	528,49 (5)	2.0 (3)	$Ca_{10}Cu_{0.04(1)}(PO_4)_6(OH)_{1.92(2)}O_{0.08(2)}$
15Cu -600	9.4156 (2)	6.88559 (9)	528.65 (1)	1.5 (3)	$Ca_{10}Cu_{0.03(1)}(PO_4)_6(OH)_{1.94(2)}O_{0.06(2)}$
15Cu-700	9,4170 (1)	6.8863 (7)	528,52 (9)	1.8 (3)	$Ca_{10}Cu_{0.04(1)}(PO_4)_6(OH)_{1.92(2)}O_{0.08(2)}$
15Cu -800	9,41765 (7)	6,8824 (4)	528,79 (5)	1.6 (3)	$Ca_{10}Cu_{0.003(1)}(PO_4)_6(OH)_{1.94(2)}O_{0.06(2)}$
15Cu -900	9,41951 (4)	6,8820 (3)	528,86 (3)	1.6 (3)	$Ca_{10}Cu_{0.03(1)}(PO_4)_6(OH)_{1.94(2)}O_{0.06(2)}$
15Cu -1000	9,41886 (3)	6,88282 (2)	528,933 (2)	2.0 (3)	$Ca_{10}Cu_{0.04(1)}(PO_4)_6(OH)_{1.92(2)}O_{0.08(2)}$
15Cu -1100	9,41749 (3)	6,88378 (2)	529,117 (2)	3.2 (3)	$Ca_{10}Cu_{0.06(1)}(PO_4)_6(OH)_{1.88(2)}O_{0.12(2)}$
15Cu -1150	9.42192 (2)	6.88531 (2)	529.339 (2)	4.9 (3)	$Ca_{10}Cu_{0.10(1)}(PO_4)_6(OH)_{1.80(2)}O_{0.20(2)}$
15Cu -1200	9.42291 (2)	6.88593 (2)	529.497 (3)	4.3 (3)	$Ca_{10}Cu_{0.09(1)}(PO_4)_6(OH)_{1.82(2)}O_{0.18(2)}$
25Cu -500	9.41974 (1)	6.88150 (1)	528.80 (1)	1.5 (3)	$Ca_{10}Cu_{0.03(1)}(PO_4)_6(OH)_{1.94(2)}O_{0.06(2)}$
25Cu -600	9.41584(1)	6.88255 (8)	528.44 (1)	1.1 (3)	$Ca_{10}Cu_{0.02(1)}(PO_4)_6(OH)_{1.96(2)}O_{0.04(2)}$
25Cu-700	9,41635(2)	6.88243 (7)	528,492 (8)	1.5 (3)	$Ca_{10}Cu_{0.03(1)}(PO_4)_6(OH)_{1.94(2)}O_{0.06(2)}$
25Cu -800	9,42051(4)	6.88325 (4)	529.02 (4)	2.0 (3)	$Ca_{10}Cu_{0.04(1)}(PO_4)_6(OH)_{1.92(2)}O_{0.08(2)}$
25Cu -900	9.41990 (3)	6.88176 (2)	528.84 (3)	1.8 (3)	$Ca_{10}Cu_{0.04(1)}(PO_4)_6(OH)_{1.92(2)}O_{0.08(2)}$
25Cu -1000	9.42032 (2)	6.88217 (2)	528.92 (3)	1.9 (3)	$Ca_{10}Cu_{0.04(1)}(PO_4)_6(OH)_{1.92(2)}O_{0.08(2)}$
25Cu -1100	9.42037 (2)	6.88304 (2)	528.99 (3)	4.8 (3)	$Ca_{10}Cu_{0.10(1)}(PO_4)_6(OH)_{1.80(2)}O_{0.20(2)}$
25Cu -1150	9.42886 (3)	6.88700 (2)	528.58 (3)	6.4 (3)	$Ca_{10}Cu_{0.13(1)}(PO_4)_6(OH)_{1.73(2)}O_{0.26(2)}$
25Cu -1200	9.42304 (3)	6.88703 (3)	529.596 (3)	6.2 (3)	$Ca_{10}Cu_{0.12(1)}(PO_4)_6(OH)_{1.76(2)}O_{0.24(2)}$
50Cu-500	9,4139 (2)	6,88385 (1)	528,33 (2)	1.3 (3)	$Ca_{10}Cu_{0.03(1)}(PO_4)_6(OH)_{1.94(2)}O_{0.06(2)}$

50Cu-600	9.41251 (1)	6.88434 (1)	528.21 (1)	1.2(3)	$Ca_{10}Cu_{0.02(1)}(PO_4)_6(OH)_{1.96(2)}O_{0.04(2)}$
50Cu-700	9,41509 (9)	6.88383 (8)	528,46 (1)	2.3 (3)	$Ca_{10}Cu_{0.05(1)}(PO_4)_6(OH)_{1.90(2)}O_{0.10(2)}$
50Cu -800	9.41920 (5)	6.88293 (4)	528.85 (5)	2.3 (3)	$Ca_{10}Cu_{0.05(1)}(PO_4)_6(OH)_{1.90(2)}O_{0.10(2)}$
50Cu -900	9.42006 (3)	6.88174 (3)	528.855 (3)	2.1 (3)	$Ca_{10}Cu_{0.04(1)}(PO_4)_6(OH)_{1.92(2)}O_{0.08(2)}$
50Cu -1000	9.42061 (3)	6.88250 (2)	528.975 (3)	2.0 (3)	$Ca_{10}Cu_{0.04(1)}(PO_4)_6(OH)_{1.92(2)}O_{0.08(2)}$
50Cu -1100	9.42062 (3)	6.88311 (3)	529.023 (3)	5.0 (3)	$Ca_{10}Cu_{0.10(1)}(PO_4)_6(OH)_{1.80(2)}O_{0.20(2)}$
50Cu -1150	9.42224 (4) 9.42992 (5)	6.88620(3) 6.89622 (4)	529.442(5) 531.077 (5)	5.8 (3) 13.7 (6)	$Ca_{10}Cu_{0.12(1)}(PO_4)_6(OH)_{1.76(2)}O_{0.24(2)}$ $Ca_{10}Cu_{0.28(1)}(PO_4)_6(OH)_{1.44(2)}O_{0.56(2)}$
50Cu -1200	9.42175 (4) 9.43046 (5)	6.88465 (3) 6.89595 (4)	529.268 (4) 531.117 (5)	4.7 (3) 13.3 (6)	$Ca_{10}Cu_{0.10(1)}(PO_4)_6(OH)_{1.80(2)}O_{0.20(2)}$ $Ca_{10}Cu_{0.27(1)}(PO_4)_6(OH)_{1.46(2)}O_{0.54(2)}$
75Cu -500	9.41696 (1)	6.88298 (1)	528.60 (1)	1.1 (3)	$Ca_{10}Cu_{0.02(1)}(PO_4)_6(OH)_{1.96(2)}O_{0.04(2)}$
75Cu -600	9.41390 (1)	6.88350 (1)	528.30 (1)	1.2 (3)	$Ca_{10}Cu_{0.02(1)}(PO_4)_6(OH)_{1.96(2)}O_{0.04(2)}$
75Cu-700	9.4157 (1)	6.88321 (8)	528.48 (1)	2.1 (3)	$Ca_{10}Cu_{0.04(1)}(PO_4)_6(OH)_{1.92(2)}O_{0.08(2)}$
75Cu -800	9.41878 (5)	6.88214 (4)	528.741 (5)	1.6 (3)	$Ca_{10}Cu_{0.03(1)}(PO_4)_6(OH)_{1.94(2)}O_{0.06(2)}$
75Cu -900	9.41997 (3)	6.88171 (3)	528.842 (3)	2.1 (3)	$Ca_{10}Cu_{0.04(1)}(PO_4)_6(OH)_{1.92(2)}O_{0.08(2)}$
75Cu -1000	9.42008 (3)	6.88201 (2)	528.878 (3)	2.2 (3)	$Ca_{10}Cu_{0.04(1)}(PO_4)_6(OH)_{1.92(2)}O_{0.08(2)}$
75Cu -1100*	9.42269 (3) 9.4326 (3)	6.88514 (3) 6.9059 (2)	529.411 (3) 532.13 (3)	3.1 (3) 21.8 (6)	$Ca_{10}Cu_{0.06(1)}(PO_4)_6(OH)_{1.88(2)}O_{0.12(2)}$ $Ca_{10}Cu_{0.44(1)}(PO_4)_6(OH)_{1.12(2)}O_{0.88(2)}$
75Cu -1150	9.42261 (5) 9.43379 (8)	6.88714 (4) 6.90985 (8)	529.555 (5) 532.564 (9)	6.7 (3) 27 (1)	$Ca_{10}Cu_{0.13(1)}(PO_4)_6(OH)_{1.74(2)}O_{0.26(2)}$ $Ca_{10}Cu_{0.54(1)}(PO_4)_6(OH)_{0.92(2)}O_{1.08(2)}$
75Cu -1200*	9.42492 (8) 9.43954 (9)	6.88839 (6) 6.91356 (7)	529.912 (8) 533.500(9)	4.8 (3) 30.4 (6)	$Ca_{10}Cu_{0.10(1)}(PO_4)_6(OH)_{1.80(2)}O_{0.20(2)}$ $Ca_{10}Cu_{0.61(1)}(PO_4)_6(OH)_{0.78(2)}O_{1.22(2)}$

* Rietveld refinement results from XRPD in transmission mode measured with capillaries.

** Cu occupancy (%) in the interstitial 2*b* Wyckoff site.

Table SEI2. Structural parameters of the β-TCP phase obtained by Rietveld refinements.

Samples	β-TCP structural parameters					
	a (Å)	*c* (Å)	*V* (Å^3)	Cu Occ in Ca4 (*)	Cu Occ in Ca5 (*)	Refined composition
00Cu-800	10.4260 (2)	37.3689 (8)	3517.85 (9)	-	-	$Ca_3(PO_4)_2$
15Cu-700	10.3925 (2)	37.3302 (8)	3491.68 (2)	25 (4)	39 (3)	$Ca_{2.82(3)}Cu_{0.18(3)}(PO_4)_2$
25Cu-700	10.38324 (2)	37.30476 (8)	3483.06 (9)	21 (6)	36 (6)	$Ca_{2.84(3)}Cu_{0.16(3)}(PO_4)_2$
50Cu-700	10.37699 (2)	37.30045 (9)	3478.46 (2)	4 (2)	48 (6)	$Ca_{2.85(3)}Cu_{0.15(3)}(PO_4)_2$
75Cu-700	10.3642 (3)	37.2859 (3)	3468.53 (8)	42 (8)	48 (6)	$Ca_{2.74(3)}Cu_{0.26(3)}(PO_4)_2$

* Cu occupancy in the Ca4 and Ca5 crystallographic site of the β-TCP structure.

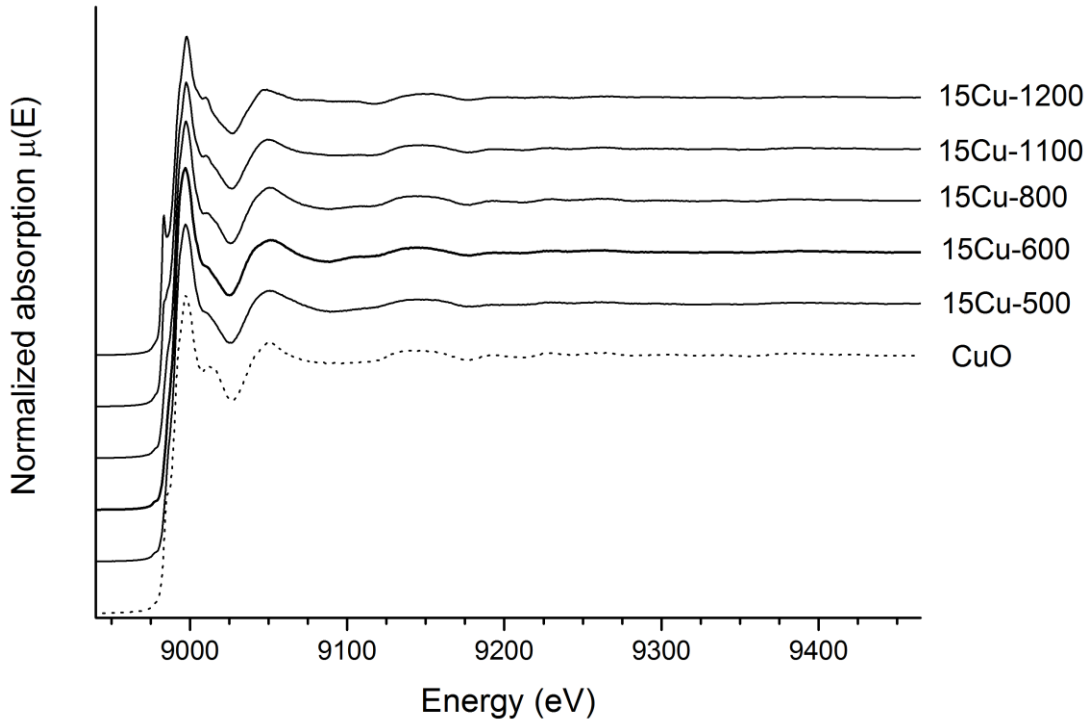

Figure SEI2. Normalized EXAFS spectra at the Cu K edge (E_0 = 8982 eV) for the 15Cu-*T* series samples (solid lines) and the reference CuO compound (dashed lines).

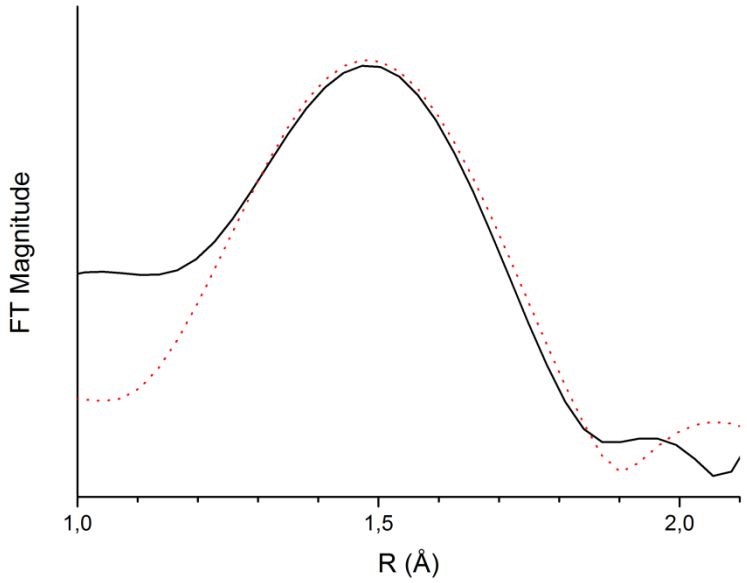

Figure SEI3. The k^3-weighted amplitude of the Fourier transform uncorrected for phase shift (black line) and best fit in *R*-space (dotted red line) for the first Cu-shell in 15Cu-1200 (independent points: 5, variables: 2, and *R*-factor: 0.0734).

Comment SEI1. XPS assignment signals.

Samples from the 75Cu-T series were analyzed by XPS spectroscopy in order to confirm the presence of Cu^{+} cations for heat treatments above 1100°C. Note that the Cu $2p_{3/2}$ signal is stable during XPS analysis, which indicates that no reduction of copper oxides takes place under the X-ray beam. In the case of copper-based compounds, reference compounds like metallic Cu, Cu_2O and CuO have to be analyzed first in order to definitively characterize formal oxidation states Cu^0, Cu^{+} and Cu^{2+} [59]. For metallic copper and Cu_2O standard samples, Cu $2p_{3/2}$ analysis reveals the presence of a peak located respectively at 932.6 eV and 932.7 eV, confirming that these two compounds cannot be precisely identified by their Cu 2p core peak position. A slight difference in the Cu 2p signature can be observed, since very weak satellite peaks are detected for the Cu_2O sample at higher binding energies, between 942.0 and 948.0 eV, associated with minor contributions from Cu d^9 initial state configurations [60], while no satellite structure is observed for metallic copper.

For the CuO sample, the main $2p_{3/2}$ peak presents a component located at 933.6 eV, attributed to Cu^{2+} atoms characteristic of the CuO phase. The other XPS peaks located at higher binding energies can be attributed to satellite peaks (940-945 eV). According to the literature [61,62], the detection of two well-separated lines (main line at 933.6 eV and satellite line in the range of 940-945 eV) can be interpreted by the occurrence of two different final states for CuO: the $3d^{10}L^{-1}$ configuration (ligand-to-metal charge transfer during the photoemission process) and the $3d^9L$ configuration (the same as the initial state). The main asymmetric line has no splitting, and is therefore ascribed to a $3d^{10}L^{-1}$ valence-band configuration since the 3d shell of the ionized copper atom is completely filled. The satellite line is quite structured and at least three components can be observed (940.8, 942.3 and 943.9 eV); it is assigned to the $3d^9L$ configuration. For this last assignment, the 3d shell of the ionized copper is partially filled and the open 2p and 3d shells will give rise to multiplet-split final, ionic, states. Finally, the Cu $2p_{3/2}$

signature of CuO is very different with respect to that of Cu_2O and Cu, as the satellite peaks at ca. 6 eV above the principal line are characteristic of Cu^{2+} in an oxygen environment. Note that Auger electrons are also created under X-ray radiation, and their corresponding peaks also contain theoretical information about the chemical environment of the element. The metallic copper Auger spectrum presents a well-resolved fine structure [60], this structure being not present for the copper oxide Auger spectra.

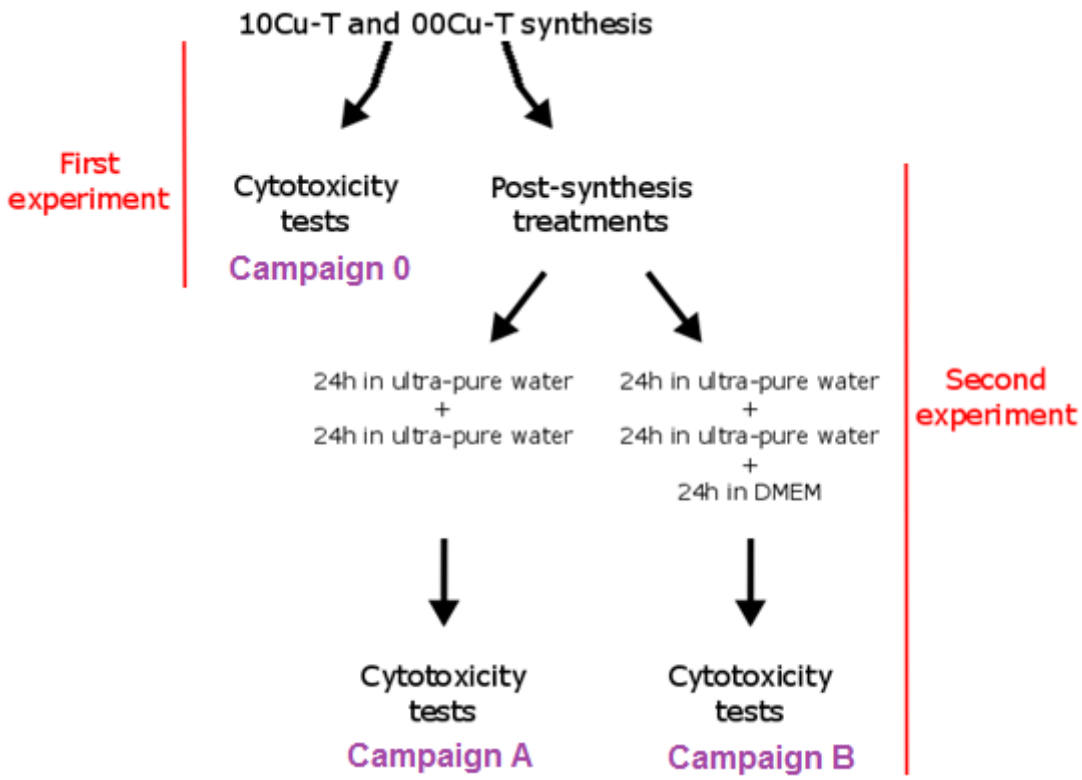

Figure SEI4. Scheme summarizing samples preparation for cytotoxicity evaluation.